

# **Structural, Opto-electronic, Electrical and Photosensing properties of Ga and Ga-Si codoped ZnO**

**M.Sc. Thesis**

By  
**Bungkiu Kissinquinker**



**DISCIPLINE OF PHYSICS  
INDIAN INSTITUTE OF TECHNOLOGY INDORE**

**June, 2020**

# **Structural, Opto-electronic, Electrical and Photosensing properties of Ga and Ga-Si codoped ZnO**

**A THESIS**

*Submitted in partial fulfillment of the  
requirements for the award of the degree  
of*  
**Master of Science**

*by*  
**Bungkiu Kissinquinker**



**DISCIPLINE OF PHYSICS  
INDIAN INSTITUTE OF TECHNOLOGY INDORE  
June, 2020**



# INDIAN INSTITUTE OF TECHNOLOGY INDORE

## CANDIDATE'S DECLARATION

I hereby certify that the work which is being presented in the thesis entitled **STRUCTURAL, OPTOELECTRONIC, ELECTRICAL AND PHOTSENSING PROPERTIES OF Ga AND Ga-Si CO-DOPED ZNO** in the partial fulfillment of the requirements for the award of the degree of **MASTER OF SCIENCE** and submitted in the **DISCIPLINE OF PHYSICS, Indian Institute of Technology Indore**, is an authentic record of my own work carried out during the time period from July 2019 to June 2020 under the supervision of Dr. Somaditya Sen, Associate Professor, Indian Institute of Technology Indore.

The matter presented in this thesis has not been submitted by me for the award of any other degree of this or any other institute.

29/06/2020

Signature of the student with date  
**Bungkiu Kissinquinker**

---

This is to certify that the above statement made by the candidate is correct to the best of my/our knowledge.

28<sup>th</sup> June 2020

**Dr. Somaditya Sen**

Signature of the Supervisor of M.Sc. thesis

---

**Bungkiu Kissinquinker** has successfully given his/her M.Sc. Oral Examination held on **22<sup>nd</sup> June 2020**

28<sup>th</sup> June 2020, **Dr. Somaditya Sen**

Signature(s) of Supervisor(s) of MSc thesis

28<sup>th</sup> June 2020, **Dr. Preeti Bhobe**

Convener, DPGC

28<sup>th</sup> June 2020, **Dr. Preeti Bhobe**

Signature of PSPC Member #1

28<sup>th</sup> June 2020, **Dr. Rajesh Kumar**

Signature of PSPC Member #2



## **ACKNOWLEDGEMENTS**

This thesis is the culmination of my journey in procuring my Master of Science (M.Sc.) degree in Physics. This journey would not have been possible without the constant support, motivation and encouragement of some people. Firstly, I would like to thank the Lord our God for all things are possible only through Him and nothing is without Him. I would like to express my sincere gratitude to my thesis supervisors Dr. Somaditya Sen who took me under his wings and has been a constant source of support and motivation. Without him this journey would not have been possible. He has always been there with valuable ideas and guidance, always ready to lend a helping hand. Dr. Somaditya Sen has been a brilliant mentor guiding me not only in my academics but also in different walks of life. His constant support, valuable advices, constructive criticism and extensive discussion helped me in accomplishing my M.Sc. Moreover, his principles, noble thoughts, fatherly care and simplicity always influenced me and will always help me in becoming a good person. It has been my privilege and honor to work with him and has been a great learning experience for me throughout my study at IIT Indore. I would like to express my sincere gratitude to my mother and my siblings for all the sacrifices they made on my behalf. My mother has always been a source of encouragement and motivation for me and her prayers have kept me going through all the difficult times in my life.

I take this opportunity to sincerely acknowledge Dr. Preeti A. Bhoje and Dr. Rajesh Kumar (PSPC) for evaluating and giving their valuable comments for improving my research work.

I want to thank whole Science department for providing all resources and facilities for accomplishing my M.Sc. thesis. I thank SIC facilities IIT Indore. I extend my grateful 'thank you' to workshop and glass blowing section for helping me fabricate the in house-experimental setup. Working

towards an M.Sc. thesis without the help of colleagues is not possible. I sincerely thank my lab mates Ruhul Amin, Koyal, Saiya Ayaz, Mohd. Nasir, Ananta Paul, Amitesh Gihar, Prashant gupta, Dr.E.G. Rini (women scientist) and all lab members for providing friendly and fulfilled environment in lab along with fruitful discussions. I would especially like to thank Prashant Kumar Mishra(PhD scholar) who has acted as a second guide for me throughout my thesis. This work would not have been accomplished without his support both academically and in the different walks of life.

I would like to take this opportunity to thank all staff member of IIT Indore for providing all comfort and convenience and also all my classmates for their moral support and academic discussions.

-----  
Bungkiu Kissinquinker

**DEDICATED TO MY LORD AND SAVIOUR  
JESUS CHRIST**

**AND**

**MY FAMILY**

## LIST OF PUBLICATIONS

### From this Thesis work: Journal Publications

[1] Prashant Kumar Mishra, Saniya Ayaz, **Bungkiu Kissinquinker**, Somaditya Sen, Defects assisted visible light sensing in  $Zn_{1-x}(GaSi)_x$   $_{2}O$ , Journal of Applied Physics 127(15):154501,(2020)

[2] Prashant Kumar Mishra, Saniya Ayaz, T. Srivastava, S. Tiwari, R. Meena, **Bungkiu Kissinquinker**, S. Biring, and S. Sen, J Mater Sci: Mater Electron **30**, 18686 (2019).

### Other work: Conference Proceedings

[1] **Bungkiu Kissinquinker**, Mohd. Nasir, Ananata Paul, Prashant Kumar Mishra, Somaditya Sen, Synthesis, optical, and electrical properties of  $Cu_{1-x}Ni_xO$ , 3RD INTERNATIONAL CONFERENCE ON CONDENSED MATTER AND APPLIED PHYSICS (ICC-2019), AIP Conference Proceedings 2220(1):140058(2020)

[2] Rini E.G., Ananta Paul, Mohd Nasir, **Bungkiu Kissinquinker**, Prashant Mishra, Somaditya Sen, Investigation of Structural and Dielectric Characteristics of  $Dy_2NiMnO_6$  Double Perovskite Ceramics, AIP Conference Proceedings 2220(1)(2020) DOI: [10.1063/5.0002281](https://doi.org/10.1063/5.0002281)

# CONTENTS

---

ACKNOWLEDGEMENT

LIST OF PUBLICATIONS

LIST OF FIGURES

ACRONYMS

## **Chapter 1: Introduction**

1.1 Crystal structure

1.2 Properties of ZnO

1.3 Intrinsic Defects in ZnO

1.4 Doping in ZnO

1.5 Applications of ZnO

1.6 Potential Functionalities of ZnO

## **Chapter 2: Experimental Technique**

2.1 Synthesis Process

2.2 Characterization Techniques

2.2.1 X-Ray Diffraction

2.2.2 UV-Vis Spectroscopy

2.2.3 Photoluminescence Spectroscopy

2.2.4 Hall effect measurement

2.3 Photo Sensing setup

## **Chapter 3: Structural Properties of pure and doped**

### **ZnO**

#### 3.1 Effect of Ga doping on structural properties of

##### ZnO

#### 3.2 Effect of Ga-Si co-doping on structural

##### properties of ZnO

## **Chapter 4: Optoelectronic properties of pure and doped**

### **ZnO**

#### 4.1 Ga-doped ZnO

##### 4.1.1 Band gap analysis

##### 4.1.2 Defect Study

#### 4.2 Ga-Si co-doped ZnO

##### 4.2.1 Band gap Analysis

##### 4.2.2 Defect study

## **Chapter 5: Electrical properties of pure and doped**

### **ZnO**

#### 5.1 Ga doped ZnO

##### 5.1.1 I-V measurements

5.1.2 Carrier properties(Hall effect  
measurements)

5.1 Ga-Si co-doped ZnO

5.2.1 I-V measurements

5.2.2 Carrier properties(Hall effect  
measurements)

## **Chapter 6: UV and Visible light sensing properties of pure and doped ZnO**

6.1 UV sensing Ga doped ZnO

6.2 UV and Visible light sensing Ga-Si co-doped  
ZnO

6.2.1 UV sensing

6.2.2 Blue light sensing

6.2.3 Green light sensing

6.2.4 Red light Sensing

## **Chapter 7: Conclusion and Future Scope**

## **REFERENCES**

## LIST OF FIGURES

Figure 1.1: The Wurtzite structure of ZnO. The tetrahedral coordination of Zn–O

Figure 1.2: Intrinsic defects in ZnO and corresponding colour emission

Figure 2.1: Sol-gel process for synthesis of ZnO

Figure 2.2: Schematic diagram showing XRD setup

Figure 2.3: Experimental set-up of UV-Vis spectroscopy

Figure 2.4: Schematic diagram for Hall probe measurement

Figure 2.5: Schematic diagram for UV to Visible light sensing setup

Figure 3.1 XRD pattern of samples Z0, ZG1, ZG3 and ZG4 showing structural resemblance to pure ZnO wurtzite  $P6_3mc$  space group

Figure 3.2: Rietveld refinement performed with  $P6_3mc$  space group for the samples Z0, ZG1, ZG3 and ZG4

Figure 3.3(a). Increase of lattice parameters  $a=b$ ,  $c$  with increasing  $x$  (b) Increasing crystallite size and decreasing lattice strain with increasing  $x$  (c, d, e) bond lengths and bond angles obtained from refined cif files of Z0, ZG1, ZG3 and ZG4

Figure 3.4: (a) XRD of  $Zn_{(1-x)}(GaSi)_xO$ , (b,c) change in lattice parameters with substitution

Figure 3.5: Variation of crystallite size and strain with doping in  $Zn_{(1-x)}(GaSi)_xO$

Figure 4.1(a) Tauc plots of substituted and parent samples showing modifications in bandedge and bandtails; (b) Bandgap increases while Urbach energy decreases with substitution

Figure 4.2(a). Energy level diagram of native defect states in ZnO (b). Modifications of the PL spectra with substitution is observed, suppressing the DLE regions and blue shifting (inset) of NBE region indicating increase of bandgap and decrease of defect states; (c). CIE representation of samples

Figure 4.3 (a, b, c and d) De-convolution of the DLE and NBE regions for all samples using Voigt distribution function

Figure 4.4 (a)  $P_N$  vs  $x$  (b)  $P_{color}$  vs  $x$  (c)  $I_{NBE}/I_{DLE}$  and  $P_{NBE}/P_{DLE}$  vs  $x$

Figure 4.5 (a) Tauc plots of  $Zn_{(1-x)}(GaSi)_{x/2}O$  ( $x=0, 0.0156, 0.0234, 0.0312$ ) showing changes in band edge and band tails or localized states; (b) Increase in Bandgap and decrease in Urbach energy with substitution  $x$

Figure 4.6 (a) Photoluminescence spectra consists of NBE and DLE regions of  $Zn_{(1-x)}(GaSi)_{x/2}O$  ( $x=0, 0.0156, 0.0234, 0.0312$ ); (b, c, d, e) deconvoluted PL spectral intensity vs energy of all samples

Figure 4.7(a) Deconvoluted PL intensity area count vs substitution  $x$  indicating variation in native defects of samples:  $Zn_{(1-x)}(GaSi)_{x/2}O$  ( $x=0, 0.0156, 0.0234, 0.0312$ ); (b) CIE plot of all samples (c) pictorial representation of energy level diagram showing native defects (in terms of wavelengths range) for all samples

Figure 5.1 (a) Increase of conductivity with increasing substitution in the regime 0-10V; inset: P-N type diode behavior of double layer pellets of ZG0 and ZG4 (b) Increase of carrier concentration ( $n$ ), conductivity ( $\sigma_{dc}$ ) and mobility ( $\mu_H$ ) with substitution; A negative Hall coefficient ( $R_H$ ) in parent ZnO (n-type semiconductor) changes sign to positive (p-type) with nominal introduction of Ga which thereafter remains positive but decreases with further substitution

Figure 5.2 (a) I-V plot with substitution  $x$  of samples (inset; the logarithmic plot of current vs voltage), (b) plot for current variation with composition for different voltage

Figure 5.3 Increase of carrier concentration ( $n$ ), conductivity ( $\sigma_{dc}$ ) and mobility ( $\mu$ ) with substitution; A negative Hall coefficient ( $R_H$ ) (n-type semiconductor) in  $Zn_{(1-x)}(GaSi)_{x/2}O$  ( $x=0, 0.0156, 0.0234, 0.0312$ )

Figure 6.1(a) Dynamic changes in current for different  $x$  (b, c) increase in  $\Delta I$  and  $I_{dark\_min}$  and decrease in sensitivity with increasing substitution (d) increasing trend of growth and decay currents with substitution (e) fast and slow response and recovery times with substitution  $x$

Figure 6.2(a, b, c, d) Variation in current w.r.t. time for different substitution  $x$ , under UV and visible lights (290nm, 450nm, 540nm, 640nm) irradiation

Figure 6.3 (b1, c1, d1, e1) shows trend of growth and decay currents vs substitution  $x$ , (b2, c2, d2, e2) shows variation of fast and slow response and recovery times vs substitution  $x$  respectively for  $Zn_{(1-x)}(GaSi)_{x/2}O$  ( $x=0, 0.0156, 0.0234, 0.0312$ )

Figure 6.4 (a) variation of sensitivity with Wavelength of  $Zn_{(1-x)}(GaSi)_{x/2}O$  ( $x=0, 0.0156, 0.0234, 0.0312$ ) ; (b) sensitivity variation with substitution  $x$  for different wavelengths (290, 450, 540 and 640)nm

## **ACRONYMS (if any)**

Zinc Oxide	ZnO
Bandgap	Eg
Urbach Energy	EU
Oxygen Vacancies	Vo
Zinc Vacancies	VZn
Zinc Interstitial	Zni
Oxygen Interstitial	Oi
Zinc antisites	Zno
Oxygen antisites	OZn
Photoluminescence	PL
Ultra Violet	UV
Visible	Vis
Diffuse reflectance spectroscopy	DRS
X-ray Diffraction	XRD



# Chapter 1

## Introduction

---

### Introduction:

Zinc Oxide is an inorganic, nontoxic and inexpensive compound of zinc and oxygen with the chemical formula ZnO. A water insoluble white powder, ZnO is found naturally as the mineral zincite but the commonly available and used ZnO is mostly synthetically produced. ZnO is classified as a (II- IV) semiconductor with a wide band gap of 3.37 eV and an excitation binding energy of 60 meV. Different synthesis routes such as sol-gel, hydrothermal, co-precipitation, wet chemical methods etc. are adopted to synthesize ZnO [1]. By adopting different synthesis methods and different precursors or by changing the conditions of synthesis different morphologies of ZnO can be synthesized such as nano rod, nano needles, nano flowers etc. The properties of ZnO can be modified by adopting different synthesis routes or by doping and codoping ZnO with other elements or compounds. This doping allows properties of ZnO such as optoelectronic, magnetic and sensing properties to be enhanced or tailored. The optical bandgap and defect states in ZnO can be tuned quite appreciably by adopting favourable synthesis conditions and dopants. This makes ZnO an interesting material for applications in optoelectronic devices with a special emphasis on its photo sensing properties in the UV to Visible range.

### 1.1 Crystal Structure:

ZnO mainly crystalizes as Cubic Zinc blend, Hexagonal *Wurtzite* and Rocksalt structure. Under ambient conditions the Hexagonal *Wurtzite* structure is the most stable thermodynamically and hence is most common[2]. In the *Wurtzite* ZnO structure, Zinc and Oxygen centres are tetrahedrally bonded with  $sp^3$  covalent bonding. The arrangement of  $O^{2-}$  and  $Zn^{2+}$  planes are such that they alternate along the c-axis. In

# Introduction

---

this structure with each  $O^{2-}$  is surrounded by four  $Zn^{2+}$  and each  $Zn^{2+}$  is surrounded by four  $O^{2-}$  (Figure 1.1). The *Wurtzite* structure of ZnO has point group  $C_{6v}$  and space group  $P6_3mc$  [2,3] with lattice parameters  $a=b=3.250 \text{ \AA}$  and  $c=5.207 \text{ \AA}$  with  $c/a \sim 1.6$  which is very close to the ideal value of 1.633 for an ideal *Wurtzite* crystal structure.

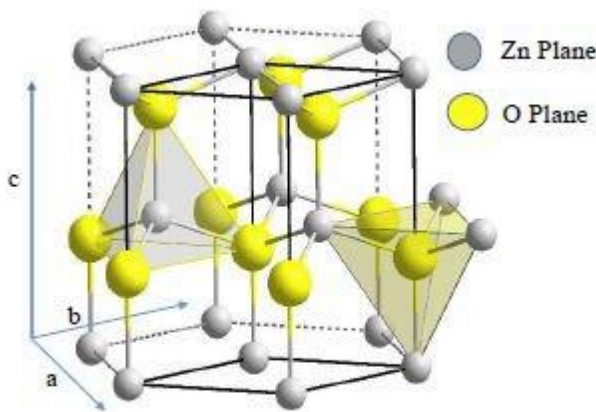


Figure 1.1: The Wurtzite structure of ZnO. The tetrahedral coordination of Zn–O

## 1.2 Properties of ZnO:

The interest in the study of any material is greatly influenced by its properties and the applicability of these properties in various fields. ZnO is a very interesting material because its properties ranging from its intriguing electrical, optical and opto-electronic properties to its mechanical properties finds applications in various fields from cosmetics and textile industries to potential applications in electronics, sensor technology and bio-medical applications. A brief description of some of the properties of ZnO is given below:

### 1.2.1 Physical Properties:

ZnO in its pure form is white in colour which on heating changes its colour to lemon yellow and on cooling turns back to white. It is odourless and has a melting point of  $1975 \text{ }^\circ\text{C}$  and a boiling point of

# Introduction

---

2360 °C with a heat capacity of 9.62cal/deg/mole at 25°C. Its molecular weight is 81.38 g/mol with a relative density of 5.607 g-cm<sup>-3</sup>.

## **1.2.2 Optical Properties:**

Pure ZnO is expected to be transparent to light in the visible region but absorbs ultra violet light. This property is due to ZnO having an optical bandgap of ~3.3eV at room temperature and ~3.44eV at temperatures of 4K[4] which corresponds to light in the UV region. This optical property of ZnO can be used for applications in photo detectors, solar cells, UV filters, etc. [4,5-7]. ZnO shows a sharp absorption peak near the vicinity of 380nm (UV region) in the photoluminescence spectra which is attributed to band to band transition and a broader emission band in the visible region which has been attributed to the intrinsic defects present in the ZnO structure.

## **1.2.3 Electrical Properties:**

ZnO is a semiconductor with n-type conductivity without unintentional doping. This n-type characteristics has been attributed to the presence of oxygen vacancies. Since ZnO being an n-type semiconductor it has a temperature dependent electron mobility with a maximum value of ~2000cm<sup>2</sup>/(V·s) at 80°C. ZnO has a direct band gap of ~ 3.3eV at room temperature which can be tuned by doping or by alloying with other metal oxides. This wide bandgap has advantages because a wide bandgap material has a high breakdown voltage, reduced electrical noise and can sustain large electric fields and also allowing operations at high power. A p-type dopant for ZnO has been one of the challenges in the study of ZnO and its property modification. A candidate for p-type dopant by modifying deep levels has been put forward in this thesis.

# Introduction

---

## 1.2.4 Opto-electronic Properties:

ZnO has a room temperature exciton binding energy of around 60 meV [8]. There is efficient excitonic emission in ZnO due to this large exciton binding energy making ZnO a potential material for applications in optical devices. The optical absorption and emission are influenced by transition related to defects which can be tuned by doping and are responsible for creating discrete electronic states in the bandgap[8]. Reports have shown green emission in photoluminescence of ZnO the origin of which has been attributed to the presence of defects such as oxygen vacancies. These defects can be tailored and in turn improves the optoelectronic properties of ZnO nanomaterials.

## 1.2.5 Mechanical Properties:

ZnO has hardness  $\sim 4.5$  on the Mohs scale and is relatively soft. ZnO nano wires have been reported to have a Young's modulus of  $\sim 50$  GPa and the modulus value for bulk scale of  $\sim 150$  Gpa[9,10] . This value of elastic constant is lower than that of other materials relevant semiconductors suchas GaN. ZnO is known to have a high heat conductivity with low thermal expansion. ZnO has been reported to have high radiation hardness which makes it applicable for conditions in high altitude or space[13,14T].

## 1.3 Intrinsic Defects in ZnO

The ZnO structure is known to have intrinsic point defects. These intrinsic point defect are: oxygen vacancies ( $V_o$ ), oxygen interstitial ( $O_i$ ), zinc vacancies ( $V_{zn}$ ), zinc interstitial ( $Zn_i$ ), oxygen antisites ( $O_{zn}$ ) and zinc antisites ( $Zn_o$ ). These defects provide levels in the band gap of ZnO and the transition from conduction bands to these levels is responsible for green, blue, violet, yellow and orange-red emission as shown in figure1.2.

# Introduction

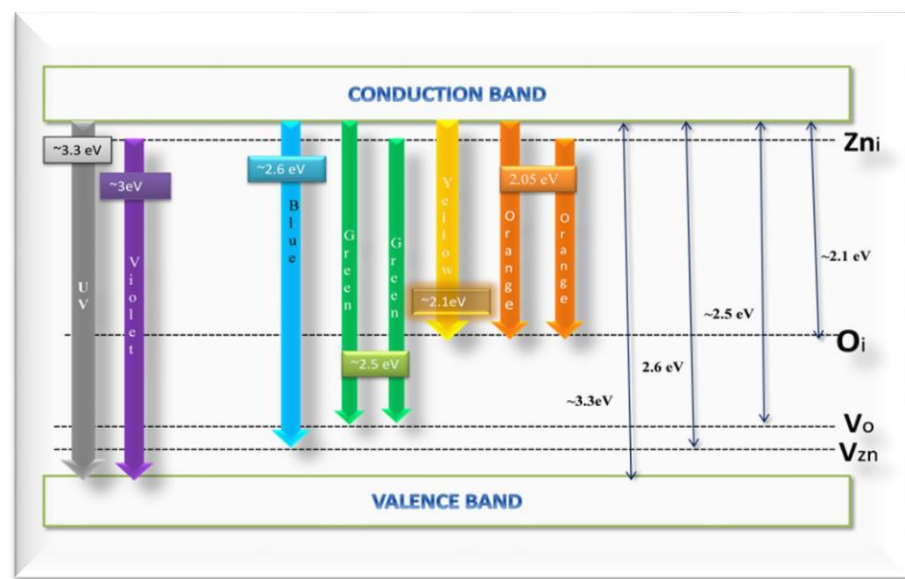


Figure 1.2: Intrinsic defects in ZnO and corresponding colour emission

### 1.3.1 Oxygen Vacancies ( $V_o$ ):

Oxygen vacancies may be conceived as the removal of an oxygen atoms which is in the  $-2$  oxidation state, from the lattice. The electrons which would normally be bound to oxygen atom which has been removed can be thought of as coming from the four neighbouring Zn sites. The electrons are still present for an uncharged defect and so there is an excess of electrons and thereby  $V_o$  is expected to behave as a donor[11].

### 1.3.2 Oxygen Interstitial ( $O_i$ ):

Two possible sites for oxygen interstitial ( $O_i$ ) in the ZnO lattice has been identified. One at the tetrahedral site and the other at the octahedral site. Tetrahedral site  $O_i$  has been found to be unstable while  $O_i$  is stable at the octahedral site. It has been reported that the  $O_i$  introduces states in the band-gap and these states are capable of accepting two electrons [11]. The transition levels introduced by  $O_i$  are located above the valance band maximum this transition state gives yellow and orange-red colour emission when an electron makes a transition from the conduction band to  $O_i$  or from transition level introduced by  $Zn_i$  to  $O_i$ .

# Introduction

---

### 1.3.3 Zinc Vacancies ( $V_{Zn}$ ):

Zinc vacancies ( $V_{Zn}$ ) can be conceived as a Zn being removed from the lattice resulting in four dangling oxygen bonds [11]. The four oxygen bonds in the valence band combine into a doubly occupied symmetric state and in the band gap as three almost degenerate states close to the valence band maxima. These three almost degenerate states has only four electrons and therefore capable of accepting two electrons. Hence,  $V_{Zn}$  shows an acceptor behavior.

### 1.3.4 Zinc Interstitial ( $Zn_i$ ):

Zinc interstitial in ZnO has two possible sites: one at the tetrahedral site and the other at the octahedral site[11]. Reports have shown that the octahedral site for  $Zn_i$  is the most stable, and that the tetrahedral site  $Zn_i$  is of a higher energy and highly unstable. At the tetrahedral site, one Zn and one O atoms are the nearest neighbours while the octahedral site, has three Zn and three O atoms as nearest neighbours. A state with two electrons is introduced above the conduction band minimum by  $Zn_i$ . The two electrons are transferred to the conduction band thereby making  $Zn_i$  a shallow donor[11]

### 1.3.5 Zinc Antisites ( $Zn_o$ ):

Zinc antisites defect originates when zinc atom is substituted at the site of the oxygen atom. Zinc anitsite has a double donor behaviour in ZnO. Zinc antisite a double donor in ZnO it might be expected that this intrinsic defect will be one of the sources of unintentional n type conductivity in ZnO. However, the high formation energy reduces its possibility for being a source of unintentional n-type conductivity[11]

# Introduction

---

## 1.3.6 Oxygen Antisites ( $O_{Zn}$ ):

Oxygen antisites ( $O_{Zn}$ ) defect originates when there is a substitution of an oxygen atom at zinc atom site. Although the oxygen antisite ( $O_{Zn}$ ) is an acceptor-type defect it has a very high formation energy and is electrically inactive even under favourable O-rich conditions. Therefore, the concentration of  $O_{Zn}$  defects are very low in ZnO at equilibrium[12].

## 1.4 Doping in ZnO

ZnO is a wide band gap semiconductor and shows mostly n-type conductivity even without any intentional doping. Doping methods conventionally used does not yield a stable p-type conductivity for ZnO. However, doping with higher or lower charged ions have been found to have a great deal of effect on the defect states and carrier concentration in ZnO. The luminescence of ZnO has been found to be adversely affected by doping. This effect on the luminescence of ZnO is due to modification of native defects of ZnO or by introduction of new defect states. Co doped ZnO shows red emission [13], Mn doped ZnO shows yellow-orange-red emission[14], Cu doped ZnO yields blue emission[15]. The effect on the carrier concentration due to doping is quite appreciable. Depending on whether the ions have a lower or higher valency than the Zn the carrier concentration have been reported to vary. Doping of elements such as Si, Ge, Sn on Zn-site have been reported for n-type conductivity in ZnO [16-20T] but reports on stable p-type dopant is sparse and an attempt has been made in this work for a p-type dopant for ZnO. The ability to alter the defect states and carrier concentration of ZnO by doping shows the workability of the material and opens up the way for a wide range of applications. Properties of ZnO can be modified, enhanced and in a sense customized to meet the need for applications in electrical, optical and opto-electronic devices.

# Introduction

---

## 1.5 Applications of ZnO

ZnO has a wide range of applications and is used in various products. In rubber manufacturing it is used in the process of vulcanization, in medicine as zinc oxide eugenol, in baby powders, lotions, ointments, sunscreen and dentistry. ZnO is used in cigarette filters to remove hydrogen cyanide and hydrogen sulfide from tobacco smoke, it is used in food industry as a necessary nutrient. ZnO also find applications in the manufacturing of paints as a pigment, and also as anticorrosive coat for metals. ZnO also finds applications in ceramic industry due to its high heat capacity, thermal conductivity and relatively low coefficient of expansion.

## 1.6 Potential functionalities of ZnO

ZnO has been reported to be a suitable material for application in electronic, opto-electronic and sensing devices. The properties of ZnO such as its structure, defect states, conductivity and bandgap determine its applications. These properties of ZnO can be altered and in a sense customized by introducing dopants which might suppress certain properties while enhancing certain others to suit the need for the functionality targeted. Below we discuss some of the functionalities of ZnO like transparent conducting oxide, UV-sensing and visible light sensing which have been probed in this work.

### 1.6.1 Transparent Conductive Oxide (TCO):

Transparent conductive oxides (TCOs) are material highly transparent to visible light and are electrically conductive. TCOs are used as transparent electrodes in Dye sensitized solar cells (DSSC) and flat panel displays such as liquid crystal displays (LCDs), plasma display panels, electronic paper displays, light-emitting-diodes (LEDs)[21],

# Introduction

---

and touch panels[22,23]. For high conductivity and transmittance a carrier concentration of the order of  $10^{20} \text{ cm}^{-3}$  or higher and a band-gap energy above 3 eV is needed [24]. Various TCOs material like impurity-doped  $\text{SnO}_2$  ( $\text{SnO}_2$ : Sb and  $\text{SnO}_2$ : F),  $\text{In}_2\text{O}_3$  ( $\text{In}_2\text{O}_3$ : Sn, or ITO), and ZnO (ZnO:Al) have been studied [25, 26]. Tin-doped indium-oxide (ITO) is the one in practical use [27,28]. However ITO is not cost efficient, Indium is not readily available and is also toxic. Thermal instability is also another issue. Hence, there is a search for an alternative material [21]. In this search for an alternative material, ZnO has been found to be a promising candidate. The pros of ZnO in comparison to ITO is that it is cost efficient, nontoxic, thermally stable and is highly durable[29]. Pure ZnO is resistive and absorbs visible light due to presence of defects in the lattice. A good choice of dopant and appropriate doping concentration can modify ZnO and hence is a promising candidate for TCOs.

## 1.6.2 UV and Visible light sensing:

Ultraviolet detection has become an important aspects of science and technology related with health, environment and even space research[30,31]. UV detectors based on silicon although available in the market are not cost efficient as they require expensive visible light filters. Faster, more sensitive, cost-effective UV detection is therefore an important research area. ZnO is easily available, cost efficient, non-toxic, does not pose a threat to the environment and has good thermal and chemical stability with high photoconductivity.

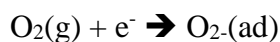
Visible light sensing can be an indispensable tool for mankind with possible applications in communication, traffic safety and automated robots. ZnO has defect levels in the band gap which can be modified by doping and changing the synthesis conditions. This modification allows for customized properties. One of the property worth exploring is the visible light sensing property of ZnO. Light in the visible region

## Introduction

---

does not have good sensitivity for pure ZnO however by modifying the defect levels UV sensitivity can be suppressed and the sensitivity to a particular colour of light enhanced. In this thesis we show enhanced red light sensing with suppressed UV sensing in co-doped samples. Pure ZnO nanoparticles normally show a relatively poor UV sensing. This is due to large n-type carrier concentration as well as fast recombination rate of photoexcited electron–hole pairs. To resolve this fundamental issue, defect engineering and doping processes have been applied to tailor certain properties of ZnO.

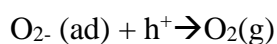
UV sensing and response in ZnO, mainly depend on the surface reaction and therefore, surface defects, grain size and oxygen adsorption properties[32–34]. The mechanism of UV sensing is based on the adsorption and desorption of Oxygen. We argue a similar mechanism for light in the visible range as well. When ZnO material is kept in the dark, the oxygen molecules get adsorbed on the surface of the ZnO by capturing free electrons from n-type ZnO



This adsorbed oxygen increases the resistance near the surface of ZnO. When the ZnO surface is illuminated by light, with energy  $h\nu$  there is generation of electron-hole pairs.



the adsorbed oxygen molecules get oxidized by the holes generated in the above process and the oxygen molecule gets desorbed from the surface of ZnO nanoparticles



This desorption from the surface increases free carrier concentration and produces a large photocurrent.

# Introduction

---

The research work reported in present thesis has been accomplished systematically in following manner

- (i) Synthesis of pure and doped ZnO samples
- (ii) Structural analysis of pure ZnO and the effect of doping on its structural properties(strain, lattice parameter etc.)
- (iii) Optical properties of ZnO such as bandgap and defect states were studied and the effect of doping/co-doping on these properties.
- iv) Investigating the electrical properties of the pure ZnO samples and the effect of doping/codoping on conductivity, carrier type, carrier concentration and mobility
- (v) Study of UV and Visible light sensing properties of pure and doped ZnO.

## Chapter 2

# Experimental Details

---

In this chapter we shall discuss in brief the process of sample preparation and the different characterization techniques used in studying the prepared samples. All the samples in this study have been prepared using sol-gel method. Characterization techniques used in this study include:

- (i) X-ray diffraction (XRD) to study the structural properties
- (ii) UV-Vis spectroscopy to study the optical band gap
- (iii) Photoluminescence spectroscopy to study the defect states and related optical properties (color emission) of the materials.

The electrical properties: I-V measurements were made using a Keithley source meter 2450 and for carrier concentration and mobility, hall effect setup was used. In house constructed setup was used for the purpose of UV and Visible light sensing.

### 2.1 Synthesis Process

The synthesis process used for synthesizing all the materials used in this study was done using the sol-gel method. A general schematic diagram for the synthesis of the nano powders is given in figure 2.1. Below a description of the nanopowder synthesis process is given for the samples used in this study.

#### 2.1.1 Synthesis of Ga doped ZnO:

Single phase homogeneous nanopowders samples with chemical composition  $Zn_{1-x}Ga_xO$  for  $x = 0$  (hereafter referred as Z0), 0.0156 (ZG1), 0.0312 (ZG3) and 0.0468 (ZG4) were synthesized using sol-gel method. A precursor solution for Zn was prepared by dissolving ZnO (Alfa Aesar, purity 99.9%) in  $HNO_3$  (Alfa Aesar, purity 99.9%). A Ga

precursor solution was prepared by dissolving gallium nitrate in DI water. The Ga solution was poured into the Zn solution and stirred for ~1hr. In a separate beaker, citric acid and ethylene glycerol were mixed in de-ionized water (DIW) and stirred for ~1hr. This solution was heated mildly to polymerize into a gelling agent. The Zn/Ga solution was then added while continuously stirring at ~70°C. The solution was heated at 70°C for ~4hrs to allow the water to evaporate and form a gel. These dehydrated gels were further heated and eventually burnt under ambient conditions to produce yellowish white powders. The yellowish white powders were then heated in a muffle furnaces at 450°C for 6 hrs to form nearly white nanopowders. The samples were then annealed at 600°C for 2 hrs in air.

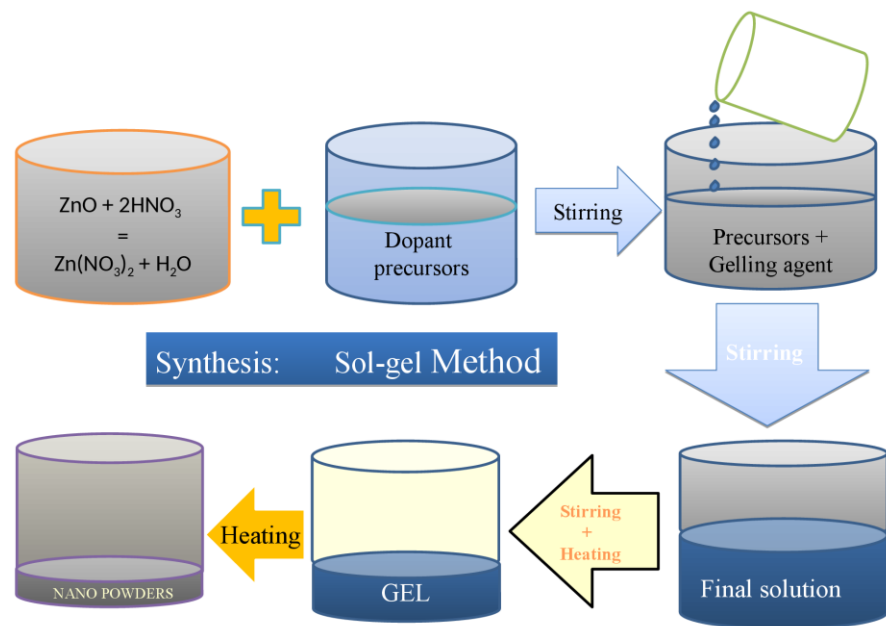


Figure 2.1: Sol-gel process for synthesis of ZnO

### 2.1.2 Synthesis of Ga-Si co-doped ZnO

$Zn_{(1-x)}(GaSi)_x/2O$  nanopowders were synthesized for  $x=0, 0.0156, 0.0234$  and  $0.0312$ .  $Ga(NO_3)_3 \cdot xH_2O$  and Tetraethyl Orthosilicate  $[(C_2H_5O)_4Si]$  were used as a precursor for  $Si^{4+}$  and  $Ga^{3+}$  respectively. Applicable quantities of both Ga and Si precursors were dissolved in

deionized water (DIW). ZnO was dissolved separately in HNO<sub>3</sub> and DIW. After thorough mixing the solution containing the dopant ions were added to ZnO dissolved separately in HNO<sub>3</sub> and DIW and vigorously stirred. Ethylene glycol and citric acid were mixed in DIW and heated at 70°C for 4hrs to obtain a polymeric solution and added to the previous solution. Finally, this solution was stirred and heated on hot plates at ~70°C for several hours to dehydrate the sol to obtain gels. Yellowish-white powders were then obtained by burning the gel on hot plates. The samples were then heated at 450°C for 6 hours and then at 600°C for 2 hours in air.

## 2.2 Characterization Technique

The samples synthesized using sol-gel route as discussed above was characterized using different characterization techniques. The characterization was done to investigate the structural, optical, electrical and sensing properties of the prepared samples. In the following section a brief description of the characterization method used is given.

### 2.2.1 X-Ray Diffraction

X-ray diffraction (XRD) is a non-destructive method of probing the d-spacing, crystal structure, lattice parameters and bond angles of the material. XRD also allows for the study of lattice strain and nano-crystalline size. Powder, pellet or film samples can be studied using XRD. The X-ray with wavelength ' $\lambda$ ' falls at an angle of incidence  $\theta$ , it undergoes diffraction by sets of atomic planes in the crystal lattice. If the d-spacing and  $\theta$  satisfies the Bragg relation

$$2d\sin\theta = n\lambda \text{ (where, n is an integer) ----- (2.1)}$$

a constructive interference takes place. The diffracted X-ray photons are then detected and counted by a detector. The X-ray falls on the sample at different angles and when the Bragg's relation is satisfied there is constructive interference and peaks are observed for that

particular value of  $\theta$  corresponding to particular sets of planes. This information from the diffraction peaks is unique for different structures and are signatures of the materials structural phase also this information is used to determine the value of d-spacing and the material being studied can be identified. The uniqueness of a set of d-values for a particular material identifies and validates the purity of a the structural phase of the material being studied.

Instrumentation of XRD:

The main components of the X-ray diffractometer are:

- i. X-ray Tube: the source of X-Rays.
- ii. Incident-beam optics: to condition the X-ray beam before it is incident on the sample
- iii. Goniometer: the platform that holds and moves the sample, optics, detector, and/or tube
- iv. Sample holder
- v. Receiving-side optics: to condition the X-ray beam after it has encountered the sample
- vi. Detector: to count the number of X Rays scattered by the sample

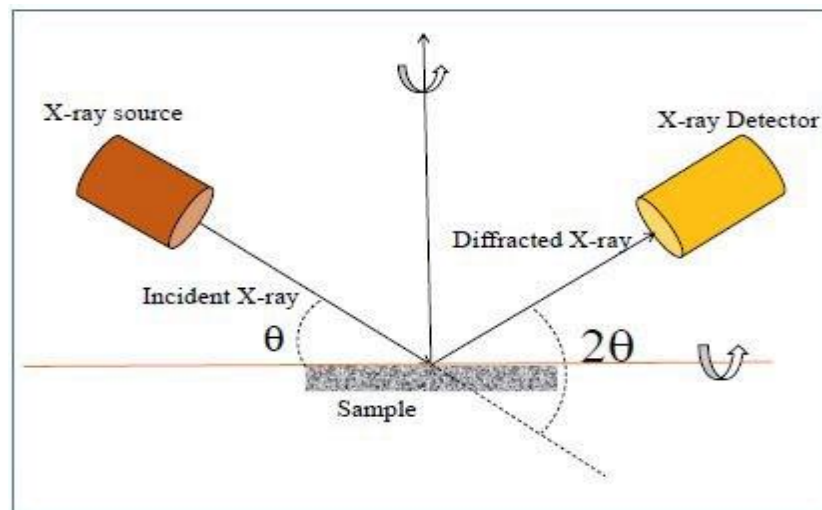


Figure 2.2: Schematic diagram showing XRD setup

Figure 2.2 shows a schematic diagram for an X-ray diffractometer with different axes of rotation. Here  $2\theta$  is the angle between the incident and diffracted beam

### 2.2.2 UV-Vis spectroscopy

When light passes through a substance, the absorption of light takes place according to the *Beer-Lambert* law

$$I = I_0 e^{-\alpha t} \text{-----(2.2)}$$

The amount of light absorbed is given by the difference between the incident radiation ( $I_0$ ) and the reflected or transmitted radiation ( $I$ ). For thickness,  $t=1$  the *Beer-Lambert* law transforms as

$$\alpha = -\ln(I/I_0) \text{----- (2.3)}$$

where,  $\alpha$  is absorbance,  $I_0$  and  $I$  are the intensities of incident and transmitted light respectively.

Experimental Set-up:

UV-Vis spectrophotometer consists of: A source of light which is usually a tungsten-halogen or deuterium lamp which is used in addition to a monochromator for selection of wavelength. The UV- visible light is converted into electrical signal with the aid of a detector. It also has a sample holder, a signal processor and a readout. Figure 2.3 shows a schematic representation of a UV-Vis Spectrophotometer.

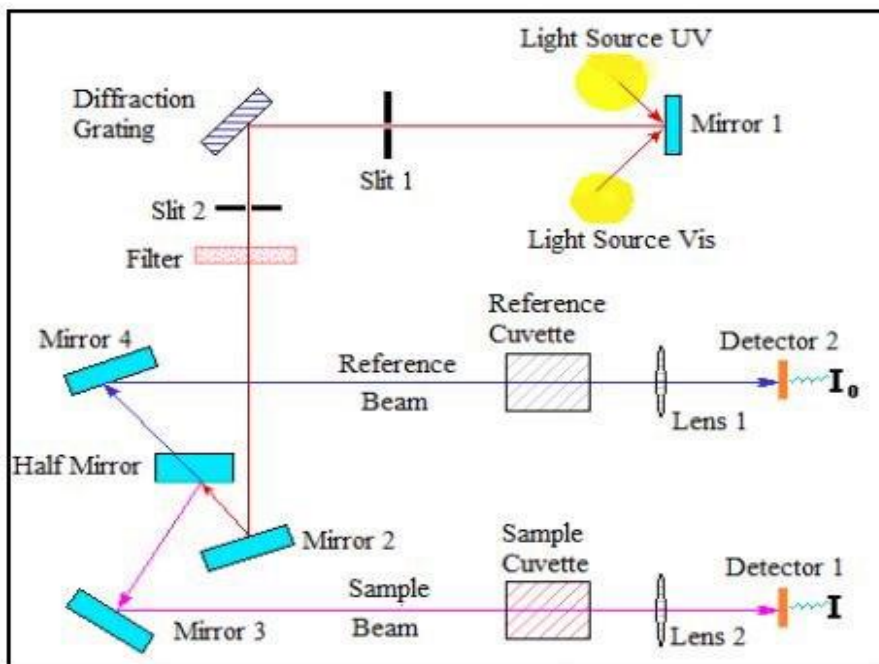


Figure 2.3: Experimental set-up of UV-Vis spectroscopy

### 2.2.3 Photoluminescence spectrometer

Photoluminescence spectroscopy is a method for investigating the defect states and electronic structure of materials[35]. A laser beam whose energy is greater than the band gap i.e.,  $E > E_g$  is made to fall on the sample. The idea behind this is that the energy which is now absorbed by the sample will dissipate when the electron makes transitions from the conduction band to the defect states or the valence band. These transitions may or may not be radiative. If the nature of the transition is radiative then there is an emission of light. The colour(wavelength) of light holds with it valuable information about the defect levels and the electronic structure of the material being studied.

The Photoluminescence spectroscopy setup consists of two main parts:

- (1) Light source which provides the energy to excite the electrons
- (2) Detection system for the photons emitted when the electron transitions to defect states or valence band.

### 2.2.4 Hall Set-up:

The Hall effect, is a phenomenon where a current carrying conductor placed in a magnetic field applied in a direction parallel to the direction of that of the current produces a voltage in a direction transverse to that of the current. The transverse voltage is induced because the charges experience a Lorentz force,

$$\mathbf{F} = q(\mathbf{E} + \mathbf{v} \times \mathbf{B})$$

This force deflects the charges on one side of the conductor producing a potential difference.

If  $V_h$  is the hall voltage, and  $I_h$  the hall current then

$$R_h = V_h / I_h$$

If  $e$  the charge associated with an electron,  $R_h$  the hall coefficient and  $n$  the number of charge carriers then, we have a relation

$$R_h = 1/ne$$

This phenomenon equation allows one to determine the carrier concentration and type of carrier from the hall effect measurements

For Hall effect measurement, a voltmeter, a constant current source, an electromagnet with provision for changing the magnetic field and a gauss meter to measure the magnetic field is required. Figure 2.4 shows a schematic diagram for hall measurements.

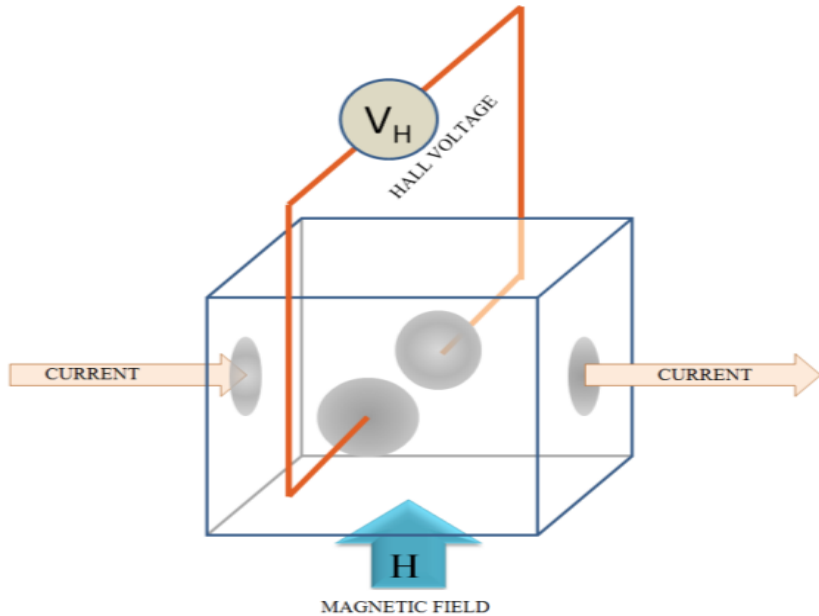


Figure 2.4: Schematic diagram for Hall probe measurement

### 2.3 Set up for UV and Visible Light sensing:

UV and Visible light sensing setup is an in house constructed setup to study the response and sensitivity of the prepared samples when exposed to light of different wavelength.

Instrumentation:

The setup consists of:

- i) UV lamp as the source of UV light of wavelength 290nm
- ii) LEDs of Red, Green and Blue colour of wavelengths 640nm, 540nm, 450nm respectively
- iii) A dark chamber to house the sample and the light source.
- iv) Arduino Uno
- v) A PC (computer)

The UV lamp and the LEDs are connected to the power source via a relay that is connected to an Arduino UNO. The Arduino can be programmed to automatically control the ON and OFF states of the light source. The sample is kept in a dark box and the light is allowed to fall on the sample. Electrodes are available so that the sample can be

connected to a multimeter or source meter. Figure 2.5 shows a schematic diagram for the UV to Visible light sensing setup along with photographs of the different wavelengths of light

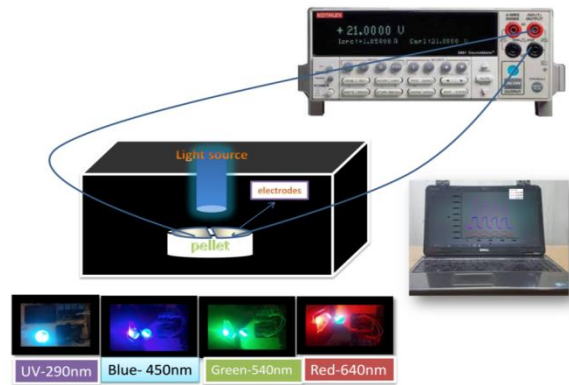


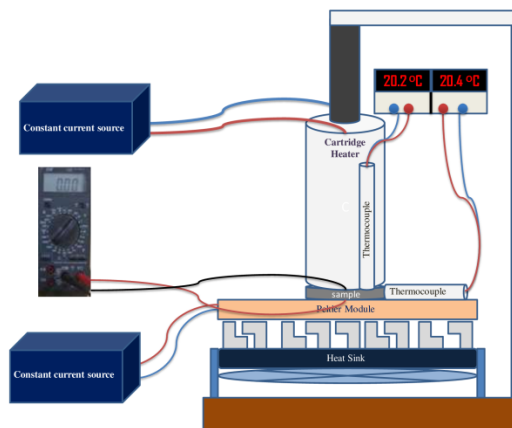
Figure 2.5: Schematic diagram for UV to Visible light sensing setup

## 2.4 Thermoelectric effect setup:

Instrumentation:

The setup consists of

- i) Peltier module and cartridge heater to generate temperature gradient
- ii) Thermocouples with digital display for temperature readings
- iii) Heat sink (CPU heat sink)
- iv) Constant current source



The setup has a peltier module and a cartridge heater which generates the temperature gradient and are each connected to a constant current source which is connected to a control knob. A 12 volt fan-cooled heat sink is used as the sink for the peltier. Two thermocouples are used to take the temperature gradient readings. The aluminium sample holder also acts as the electrodes which can be connected to a multimeter.

## Chapter 3

# Structural properties of pure and doped ZnO

In this chapter we shall discuss the structural properties of pure ZnO and the effect of Gallium (Ga) doping and Gallium-Silicon (Ga-Si) co-doping on the structure studies through X-Ray Diffraction analysis. X-ray diffraction (XRD) was performed on the synthesized nanoparticles using Bruker D2-Phaser diffractometer with Cu anode. The X-ray tube had a radiation of wavelength  $\sim 1.5406\text{\AA}$ .

### 3.1 Effect of Ga doping on Structural properties of ZnO

XRD spectra showed a single phase structure for all the samples  $\text{Zn}_{1-x}\text{Ga}_x\text{O}$  for  $x = 0$  (hereafter referred as Z0), 0.0156 (ZG1), 0.0312 (ZG3) and 0.0468 (ZG4) without the presence of any secondary phase. The XRD spectra is shown in Figure 3.1.

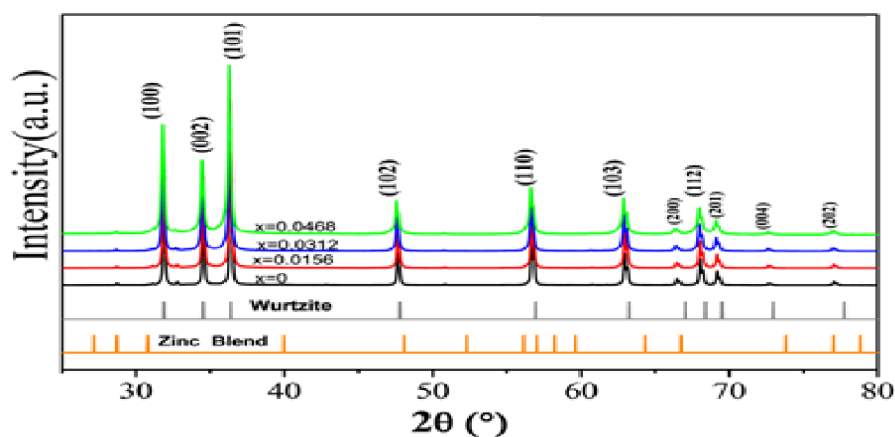


Figure 3.1 XRD pattern of samples Z0, ZG1, ZG3 and ZG4 showing structural resemblance to pure ZnO wurtzite  $P6_3mc$  space group

Rietveld refinement of the XRD data was performed using GSAS software, and it revealed a *wurtzite*  $P6_3mc$  space group as shown in Figure 3.2(a, b, c, d). Lattice parameters  $a$  ( $=b$ ) showed an nominal increasing trend while  $c$  increased with substitution [Figure 3.3(a)].

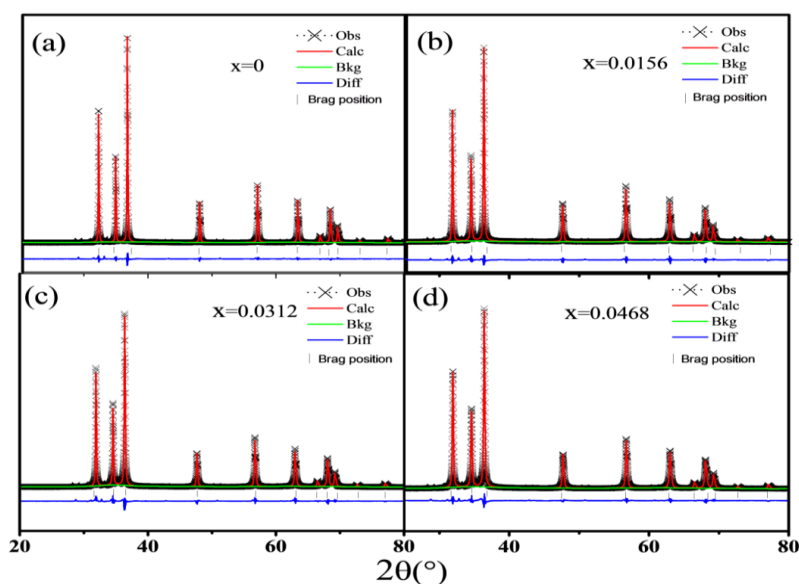


Figure 3.2: Rietveld refinement performed with  $P6_3mc$  space group for the samples Z0, ZG1, ZG3 and ZG4

Peaks corresponding to (002) showed a shift [Figure 3.1 (inset: (002) peaks)] indicating change in  $c$  parameter. Crystallite size was estimated using Debye Scherrer equation,  $D = 18,000\lambda / (\pi L_x)$ , while strain was calculated using  $S = (\pi L_y) / 18,000$ , where,  $L_x$  and  $L_y$  were obtained from Rietveld refinement. The crystallite size of the particles increased from 38 nm to 46 nm with increasing Ga-content. On the other hand the lattice strain decreased with increasing Ga-content from 0.33% to 0.29%. Bond lengths and bond angles were also estimated from the refined cif files show in Figure 3(c, d, and e). The Zn-O bond length along  $c$ -axis for ZG1 increases by  $\sim 1.1\%$  compared to Z0. However, with further substitution, the bond lengths start decreasing for ZG3 and ZG4. The Wyckoff position and occupancy is given below:

Samples	Zn				O				Ga			
	Wyckoff position			occ	Wyckoff position			occ	Wyckoff position			occ
x=0	0.33	0.66	0.49	1.0000	0.66	0.33	0.37	1.0000				0.0000
X=0.015 6	0.03	0.66	0.50	0.5076	0.66	0.33	0.39	1.0000	0.33	0.66	0.5219	0.0156
X=0.031 2	0.33	0.66	0.05	0.9688	0.66	0.33	0.17	1.0000	0.33	0.66	0.0526	0.0312
X=0.046 8	0.33	0.66	0.49	0.9532	0.66	0.33	0.37	1.0000	0.33	0.66	0.4961	0.0468

It may be noted, that for ZG4 this bond length is actually smaller than Z0. On the other hand the bond length not along a/b axes decrease by 0.3% for ZG1 and thereafter start to increase for ZG4 this bond length is more than Z0. The Ga-O bond lengths along the c-axis are smaller than similar Zn-O bond lengths along c-axis of the corresponding samples and also of a pure ZnO. On the other hand the Ga-O bond lengths angular to the c-axis are larger than their corresponding Zn-O bond lengths. Bond angles also follow a similar trend [Figure 3.3(e)].

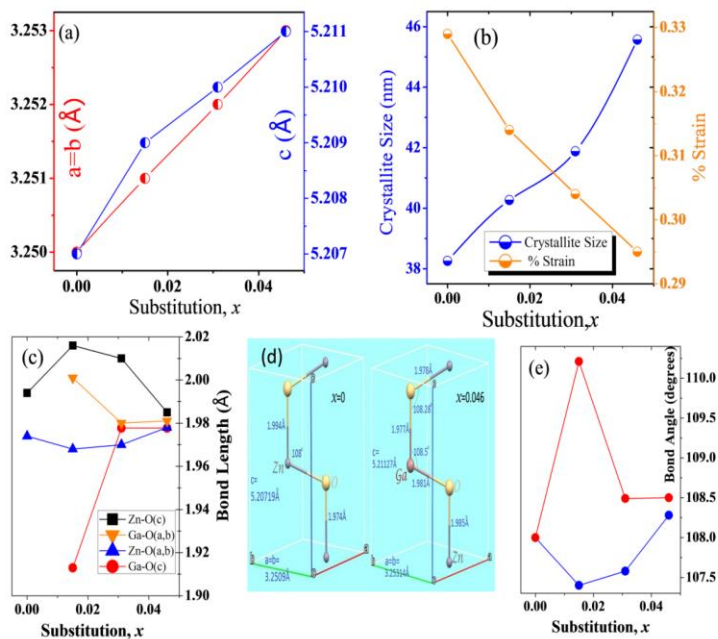


Figure 3.3(a). Increase of lattice parameters  $a=b$ ,  $c$  with increasing  $x$  (b) Increasing crystallite size and decreasing lattice strain with increasing  $x$  (c, d, e) bond lengths and bond angles obtained from refined cif files of Z0, ZG1, ZG3 and ZG4

### 3.2 Effect of Ga-Si co doping on structural properties of ZnO

XRD patterns confirm a hexagonal *wurtzite* ZnO structure for all the samples annealed at 600°C. It shows some nominal traces of *zinc-blende* phase which is due to the precursor material. No extra phases other than the *wurtzite* ZnO are observed related to any complex mixed oxides of Zn, Ga or Si [Figure 3.4(a)]. Rietveld refinement was performed for all the samples using GSAS software to estimate the

structural properties of the samples. Lattice parameters ( $a = b$ ) and  $c$  decreases with substitution [Figure 3.1(b, c)].

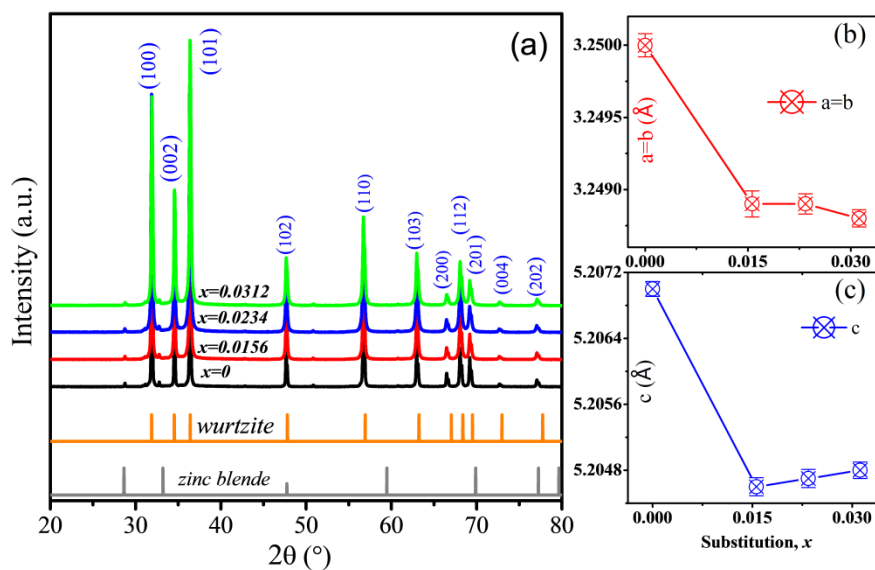


Figure 3.4: (a) XRD of  $Zn_{(1-x)}(GaSi)_{x/2}O$ , (b,c) change in lattice parameters with substitution

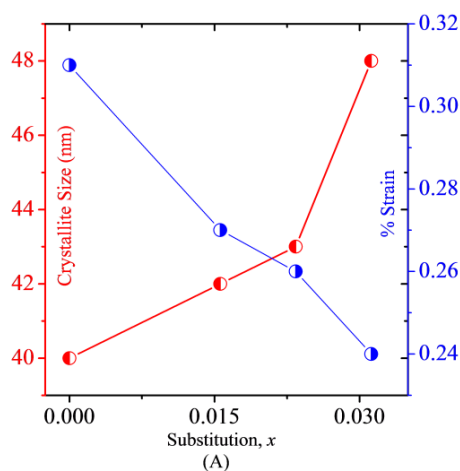


Figure 3.5: Variation of crystallite size and strain with doping in  $Zn_{(1-x)}(GaSi)_{x/2}O$

Nominal changes in lattice parameters ( $a$ ,  $b$  and  $c$ ) were observed in the third decimal digit. The ionic radii of the dopants,  $Ga^{3+}$  (0.62 Å) and  $Si^{4+}$  (0.40 Å) are smaller than that of  $Zn^{2+}$  (0.74 Å). Hence, from the aspect of ionic size such a lattice contraction is logical. However, an enhancement in cationic charge may introduce excess oxygen to satisfy charge balance in the lattice. This may create oxygen

interstitials which can result in lattice expansion. Such factors influence bond lengths and bond angles which can be related to lattice strain [20,38,39]. The crystallite size was found to decrease with concentration with increase in strain as shown in figure 3.5.

## Chapter 4

### Optical properties of pure and doped ZnO

---

Zinc oxide (ZnO) is recognized as a II–VI photonic semiconductor materials with a wide band gap ( $\sim 3.37$  eV) and high exciton binding energy ( $\sim 60$  meV)[4]. It is a potential material for applications in optoelectronic devices such as UV lasers, gas and bio sensors. Wide range of properties of doped ZnO[64] depends on defects and associated charge carriers that are possible in these materials. The customization of these properties plays an important role in the applicability of ZnO.

The pure and doped ZnO samples were studied for their optical properties. The study involved studying its bandgap and defect levels using UV-vis spectroscopy and photoluminescence spectroscopy.

#### 4.1 Ga doped ZnO

##### 4.1.1 Bandgap analysis

From the room temperature optical absorbance data [Figure 4.1(a)], the bandgap ( $E_g$ ) was estimated using a Tauc plot by extrapolating the linear part of graph between  $(\alpha h\nu)^2$  Vs  $h\nu$  [47].

$$[\alpha h\nu = A (h\nu - E_g)^n]$$

where,  $\alpha$  is the absorption coefficient,  $A$  is a constant,  $h\nu$  is the energy of the incident light and  $n$  is a constant ( $n=1/2$  for direct and  $n=2$  for indirect bandgap). Urbach energy ( $E_U$ ), an estimate of lattice disorder [8,9,26], was calculated from the slopes of  $\ln(\alpha)$  versus  $h\nu$  graph where,  $\alpha = \alpha_0 \exp(h\nu/E_U)$ , where,  $\alpha_0$  is a constant. Enhancement in  $E_g$  is observed with Ga doping, from  $\sim 3.21$  eV (Z0) to 3.28 eV (ZG4), while  $E_U$  decreases from  $\sim 92.5$  meV (ZG0) to 72.5 meV (ZG4) [Figure 4.1(b)]. Hence, it seems, Ga doping helps reduce the strain and stabilize the structure by reducing lattice disorder.

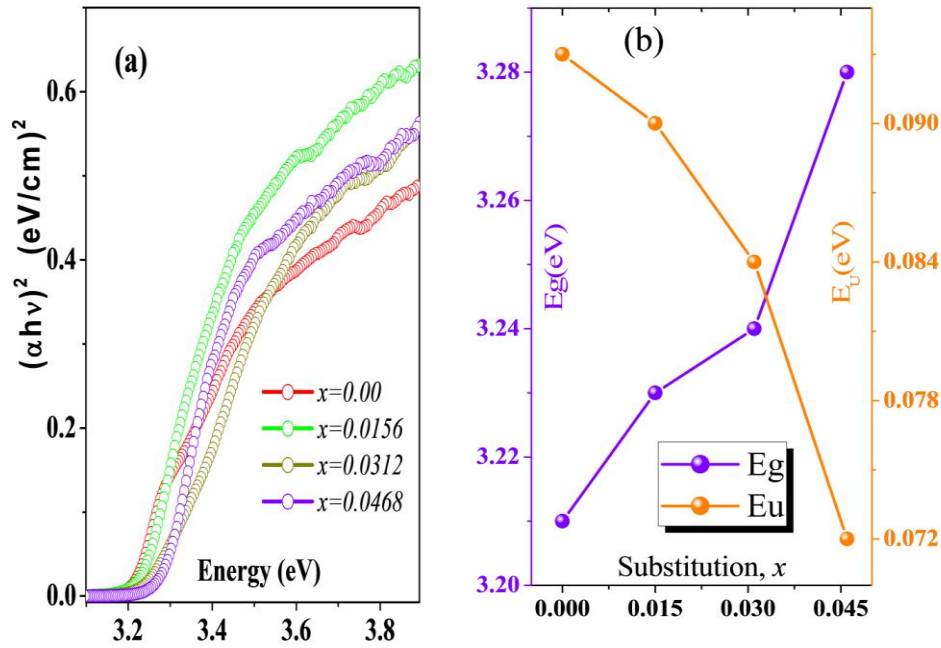


Figure 4.1(a) Tauc plots of substituted and parent samples showing modifications in bandedge and bandtails; (b) Bandgap increases while Urbach energy decreases with substitution

#### 4.1.2 Defect study

The PL spectra comprised of NBE (near band emission, i.e. UV part) and DLE (deep level emission, i.e. visible color emission) [Figure 4.2(b)]. The DLE and NBE spectra were deconvoluted [48–53] into various emission peaks in different colour regions [Figure 4.3(a, b, c, d)], e.g. UV (>3.1 eV), violet (~3–3.1 eV), blue (2.50–2.75 eV) [21, 22, 54], green (2.17–2.50 eV) [55,15-20], yellow (2.10–2.17 eV) and orange-red (2.1 eV) [26,56,57]. These emissions correspond to various defects, e.g.,  $Zn_i$  (violet) [55, 58],  $V_O$  (green),  $O_i$  (yellow, orange-red), and  $V_{Zn}$  (blue), located below the CB at ~0.22 eV, ~2.5 eV, ~2.28 eV, and ~2.85 eV respectively. The energy level diagram of native defect states in ZnO is shown in Figure 4.2(a).

The area under the curve in the DLE region decreased with Ga doping, indicating a reduction in defect states [Figure 4.2(b)]. The gradual shift of the NBE to higher energy [Figure 4.2(b) inset], confirms the changes in  $E_g$  in agreement with UV-Vis spectroscopy results. Area calculation of each peak provides information on color

contribution [26]. The proportion of each color in PL spectrum is estimated as  $P_{\text{color}}=A_{\text{color}}/A_{\text{total}}$  [Figure 4.4(b)], such that  $A_{\text{total}}=\Sigma A_{\text{color}}$  and,  $\Sigma P_{\text{color}}=1$ . Individual color contributions,  $P_{\text{color}}$ , have been normalized with respect to  $P_{\text{UV}}$ , to yield  $P_{\text{N}}(=P_{\text{color}}/P_{\text{UV}})$  [Figure 8(a)], assuming UV contribution is constant for all samples which is a contribution of a  $\text{CB}\rightarrow\text{VB}$  transition.

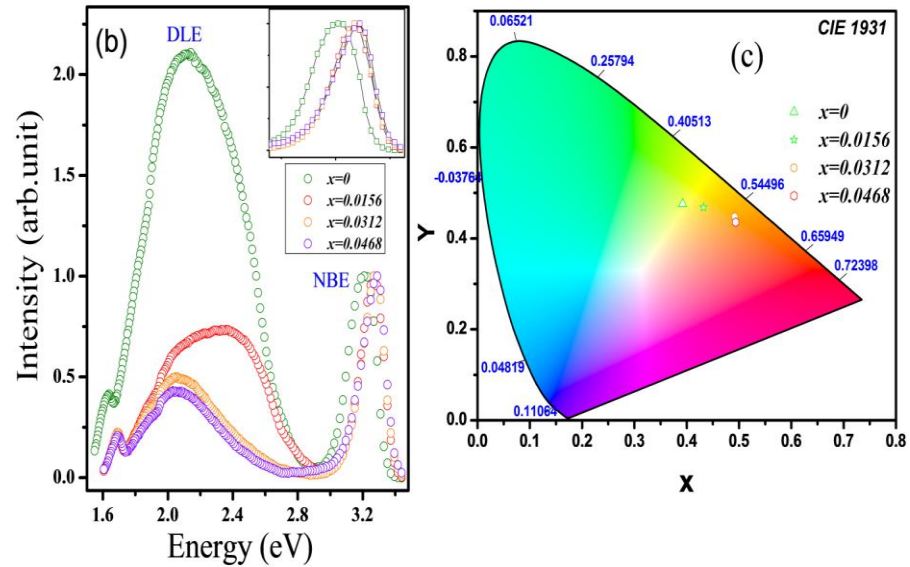


Figure 4.2(a). Energy level diagram of native defect states in ZnO (b).Modifications of the PL spectra with substitution is observed, suppressing the DLE regions and blue shifting (inset) of NBE region indicating increase of bandgap and decrease of defect states; (c). CIE representation of samples

It is observed that  $P_{\text{N}}$  decreases for green and orange-red colors. The decrease in green color intensity hints at a reduction in latent  $\text{V}_{\text{O}}$  [22, 59–62]. Notably, latent  $\text{O}_{\text{i}}$  (orange-red emission) decreases at par  $\text{V}_{\text{O}}$  [15–20, 26, 63, and 64]. Hence, the latent  $\text{O}_{\text{i}}$  present may be filling up the latent  $\text{V}_{\text{O}}$  present in pure ZnO.  $\text{Zn}_{\text{i}}$  (presence of violet emission) is present in ZG3 and ZG4.  $\text{V}_{\text{Zn}}$  (blue emission) are present in ZG0 and increases in ZG1 samples but nearly vanishes in ZG3 and ZG4. Yellow emission too shows such a fluctuating nature and decreases drastically for ZG1 but thereafter increases for ZG3 and ZG4 respectively.

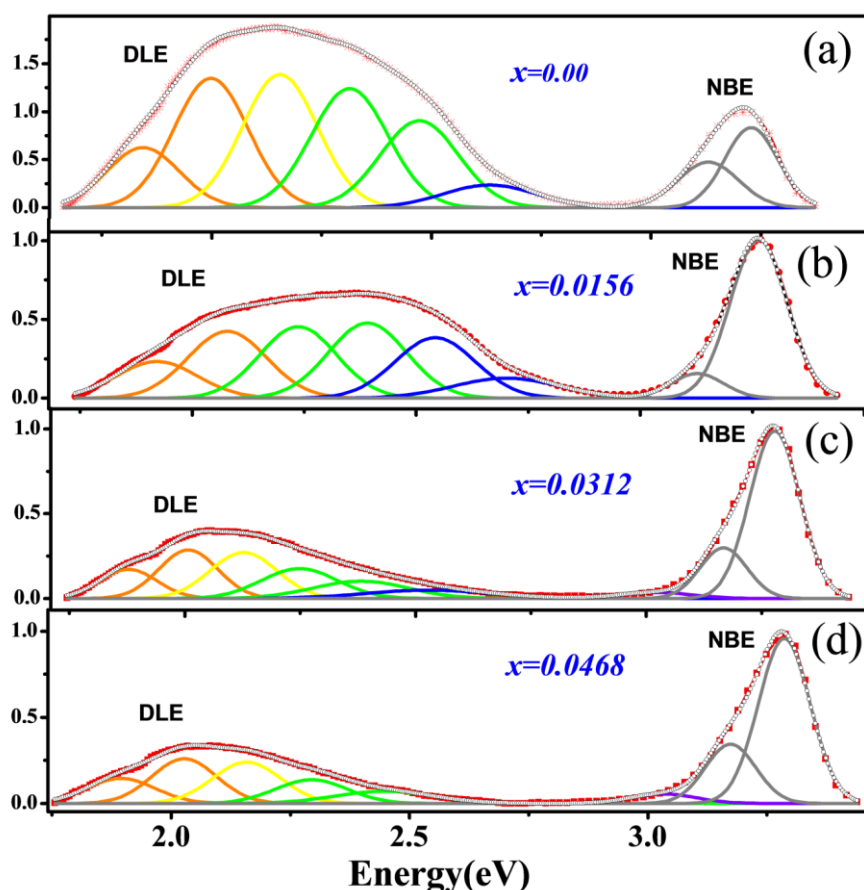


Figure 4.3 (a, b, c and d) De-convolution of the DLE and NBE regions for all samples using Voigt distribution function

The inverse trends between  $V_{Zn}$  and  $O_i$  tempt one to believe that these  $O_i$  were actually occupying a position adjacent to a Zn-site in the pure ZnO, which by the substitution of a smaller  $Ga^{3+}$  ion ( $0.62 \text{ \AA}$ ) has been rearranged. Beyond ZG1, the extra charges of  $Ga^{3+}$  ions may attract excess O ions, which will result in  $O_i$ , in the vicinity of a comparably more attractive  $Ga^{3+}$ , thereby filling in the  $V_{Zn}$  [Figure 4.4(a)].

A ‘Commission Internationale d’Eclairage’ (CIE 1931 standard) chromaticity color graph was calculated using OSA software. Chromaticity coordinates obtained were as follows: Z0 (0.39, 0.47), ZG1 (0.43, 0.46), ZG3 (0.49, 0.44) and ZG4 (0.49, 0.43) [Figure 4.2(b)]. A drastic coordinate shift towards orange-red emission is observed for ZG3 and further for ZG4. Shifting of coordinates is probably due to a proportionate reduction of  $V_O$  and  $O_i$ , and the

simultaneous extra addition of newly created  $O_i$  due to the extra charge of the substituent  $Ga^{3+}$ . Therefore, it can be inferred that all sorts of latent defects reduce with Ga doping while  $Ga^{3+}$  associated  $O_i$  increases for ZG3. Both  $I_{NBE}/I_{DLE}$  (intensity ratio) and  $P_{NBE}/P_{DLE}$  (color ratio) ratios increase with  $Ga^{3+}$  substitution which indicates latent defects suppression [Figure 4.4(c)]. This agrees with UV-Vis studies.

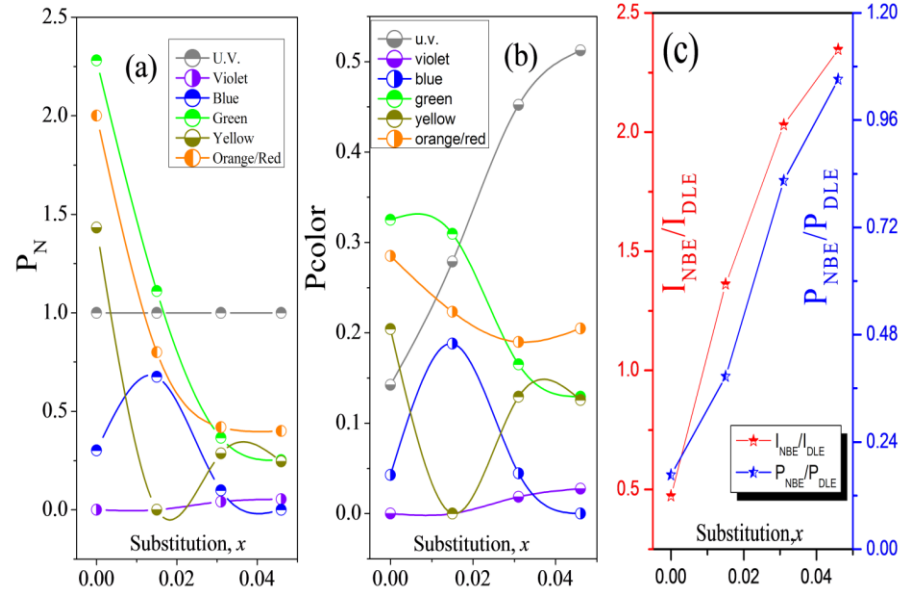


Figure 4.4 (a)  $P_N$  vs  $x$  (b)  $P_{color}$  vs  $x$  (c)  $I_{NBE}/I_{DLE}$  and  $P_{NBE}/P_{DLE}$  vs  $x$

## 4.2 Ga-Si doped ZnO

### 4.2.1 Bandgap Analysis

The optical bandgap was calculated from energy-dependent optical absorbance data [Figure 4(a)] using Tauc method [37,44–48]. Davis and Mott further expressed the relation between optical absorption and the difference between photon energy and bandgap as:

$$(\alpha h\nu)^{1/n} = A(h\nu - E_g) \quad [44,45,49]$$

where,  $\alpha$  is the absorption coefficient,  $\nu$  the photon's frequency,  $h$  the Planck's constant,  $A$  is a proportionality constant and  $E_g$  is the bandgap. The power coefficient  $n$  determines the nature of transition between CB and VB:  $n = 1/2, 3/2, 2,$  and  $3$  for direct allowed, direct forbidden, indirect allowed and indirect forbidden transitions, respectively. The direct bandgap ( $n=1/2$ ) of

ZnO increases slightly with Ga<sup>3+</sup>/Si<sup>4+</sup> co-doping from ~3.21 eV (Z0) to ~3.25 eV (ZSGO3). Such an increase of bandgap has been discussed in literature [9,37,48,50–53] as a result of Burstein-Moss effect, in which states are created in the conduction band very close to the conduction band edge with degenerate energy levels exceeding the density of states of the conduction band edge. Such degenerate states shift the Fermi level into the conduction band. This imitates an Ohmic nature of the samples giving rise to the linear nature of the I-V characteristics. The bandgap can also be modified due to modifications in the lattice strain in a defective semiconductor.

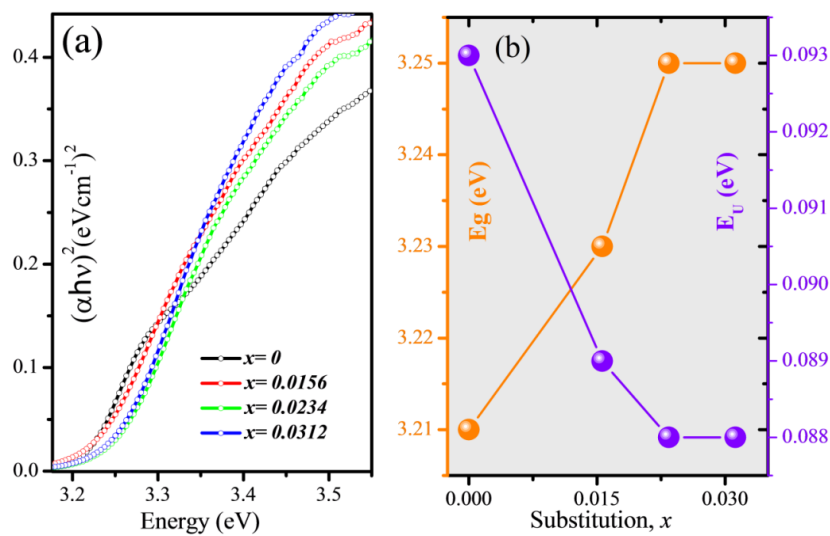


Figure 4.5 (a) Tauc plots of Zn<sub>(1-x)</sub>(GaSi)<sub>x/2</sub>O ( $x=0, 0.0156, 0.0234, 0.0312$ ) showing changes in bandedge and band tails or localized states; (b) Increase in Bandgap and decrease in Urbach energy with substitution  $x$

Certain localized defect states (disorderness, lack of crystallinity, etc.) are formed just below the conduction band or above the valence bands resulting in induced band-tails (Urbach tail). A reduction of structural strain can reduce band-tailing. The gap between the available electronic states near the band edges therefore increases, thereby increasing the bandgap when lattice strain decreases. Urbach band-tail energy,  $E_U$ , was estimated from the slope of logarithmic plots of  $\ln[\alpha]$  and  $h\nu$  as:

$$\ln[\alpha] = \ln[\alpha_0] + (h\nu/E_U) \quad [44, 45, 54-56]$$

Where,  $\alpha_0$  is a constant,  $E_U$  is the Urbach energy of the band tail. With increasing substitution the  $E_U$  nominal decreases from  $\sim 93$  meV (Z0) to  $\sim 88$  meV (ZSGO3). Hence, with increasing substitution the lattice strain ( $E_U$ ) becomes less strained and there by results in nominal increase in  $E_g$ .

### **Defect study:**

Information on the defect states located inside the band-edges was extracted from the photoluminescence (PL) spectra of the ZSGO samples [Figure 5(a)]. The PL spectra of ZnO has been discussed in literature as composed of Deep Level Emission (DLE:  $\sim$ ranging from  $\sim 387$  nm ( $\sim 3$  eV) to  $\sim 738$  nm (1.6 eV) and the Near Band-Edge Emission (NBE: a sharp feature  $\sim 375$  to  $380$  ( $\sim 3.2$  eV) nm regions [25,45,49,57–62]).

In literature, there are several controversial claims about defects centres and corresponding energy levels in ZnO band structure, especially in the DLE region. Janotti and Van de Walle described this in detail for individual defect types including Zn interstitials ( $Zn_i$ ), Oxygen interstitials ( $O_i$ ), Zn vacancies ( $V_{Zn}$ ), O vacancies ( $V_O$ ), Zn antisites ( $Zn_O$ ), O antisites ( $O_{Zn}$ ), etc[11,12]. The entire controversy was discussed and different theoretical references were detailed including their own work.

It was observed that  $Zn_i$  can be expressed as a deep donor with transition levels  $\sim 0.5$  eV above the valence band (VB). At the same time, there are reports of  $Zn_i$  as a shallow donor close to the CB.  $Zn_i$  defect states have also been reported at  $\sim 0.22$  eV below the conduction band [12,63,64]. Electronic structure of the simulated ZnO structure revealed that  $Zn_i$  states can be well inside the CB ( $\sim 1.2$  eV above the CB edge) thereby allowing an n-type conductivity. However, a majority of reports have observed  $Zn_i$  about  $\sim 0.2$  eV below the CB edge.[9,14,63–65] Hence, taking these major trends into account one can allot the  $Zn_i$  defect states in a band  $\sim 0.2$  eV below the CB edge,

which allows a transition to the VB with energy  $\sim 2.75\text{-}3\text{eV}$  ( $\sim 387\text{-}460\text{nm}$ ) producing a violet luminescence.

$V_{\text{Zn}}$  states can occur in two different charge states above the VB with a difference of around  $\sim 0.8\text{ eV}$ . Himanshi et al. reported  $V_{\text{Zn}}$  states at  $\sim 2.51\text{-}2.60\text{ eV}$  below to CB [11,24,49,66]. Similar  $V_{\text{Zn}}$  defect states have been reported at  $\sim 2.60$  to  $\sim 2.77\text{eV}$  below the CB. Tengfei et al. reported  $V_{\text{Zn}}$  at  $\sim 2.84$  below the CB [46,47,67]etc. Hence, majority reports hint at  $V_{\text{Zn}}$  states, that allows  $\text{CB} \rightarrow V_{\text{Zn}}$  transitions in an energy band of  $\sim 2.5\text{-}2.84\text{eV}$  ( $387\text{ nm}$  to  $460\text{ nm}$ ) resulting in blue emission.

$O_i$  defect states have been reported at  $\sim 1.96\text{eV}$  above the VB. Djurišić et al. reported a similar  $O_i$  defect state  $\sim 1.93\text{eV}$  above the VB[62]. Similar multiple reports claimed  $O_i$  defect states  $\sim 1.70\text{-}2.10\text{ eV}$  ( $\sim 729$  to  $590\text{nm}$ ) above the VB [9,37,49,64,66,68]. These defect levels allow a transition to the VB, allowing an orange emission. However,  $O_i$  defects have also been located at a higher energy state  $\sim 2.15\text{eV}$ . Transitions from these defect states to the VB results in yellow emission  $\sim 2.15\text{eV}$  ( $\sim 575\text{nm}$ ). As the majority of  $O_i$  defects have been discussed in literature as located in the range  $\sim 1.95$  to  $2.15\text{ eV}$  ( $\sim 635$  to  $\sim 576\text{nm}$ ) and can be related to orange to yellow type of emissions.

Similarly, in the case of  $V_{\text{O}}$  states have been reported at  $\sim 2.50\text{eV}$  above the VB. However, Janotti et al. has reported deep level  $V_{\text{O}}$  defects states at  $1.0\text{ eV}$  below the CB edge. Others have reported levels  $\sim 2.4\text{ eV}$  below the CB edge. Other similar supporting reports are available at  $\sim 2.4$  to  $\sim 2.5\text{ eV}$  below the CB edge. Hence, there is a majority of reports [9,12,63,64,69–75] referring to  $V_{\text{O}}$  defect levels at  $\sim 2.2$  to  $2.5\text{ eV}$  below the CB edge. Hence, taking these major trends into account one can allot the  $V_{\text{O}}$  defect states as a band ranging from  $\sim 2.20$  to  $2.50\text{ eV}$  ( $\sim 563$  to  $\sim 496\text{nm}$ ) below CB edge which incidentally represents a green luminescence.

Kohan et al. and Zhang et al. reported  $\text{ZnO}$  antisite defect states located at  $\sim 1.45\text{eV}$  above VB [63,65]. These states are at a higher energy level than  $V_{\text{O}}$  and  $\text{Zn}_i$ . However, Oba et al. found that  $\text{ZnO}$  energy states to be comparable with  $V_{\text{O}}$  defects in a Zn-rich lattice[64]. However, these

states have different charges and the energy levels can vary accordingly. Janotti reported a shallow donor-type nature of  $Zn_O$  for a stable +2 charge state with energy levels above CB edge[12]. Since the formation energy of  $Zn_O$  is very high it is unlikely to attain equilibrium with a Fermi level in between bandgap. Hence, Oba et al. has mentioned that  $Zn_O$  states (similar to  $Zn_i$  states) can be well inside the CB ( $\sim 1.2$  eV above the CB edge) thereby allowing an n-type conductivity [64]. The  $Zn_O$  defects, thereby, can be related to an increase and an Ohmic nature of conductive properties, but not significant to DLE. However,  $O_{zn}$  is an acceptor type point-defect with very high formation energy. Hence, even in the presence of O-rich conditions, it is unlikely to find a significant and detectable amount of  $O_{zn}$  [63,64]. Hence, the contribution of such types of antisite defects in DLE is minimum. Hence, based on the above discussion, the DLE region can be deconvoluted [Figure 5(b, c, d, and e)] into several peaks corresponding to different color emissions from different defects. This includes  $Zn_i$ : violet emission  $\sim 2.75$ - $3$ eV ( $\sim 450$  to  $\sim 413$ nm),  $V_{Zn}$ : blue emission  $\sim 2.75$ - $2.50$ eV ( $\sim 450$ nm to  $496$ nm),  $O_i$ : yellow  $\sim 1.65$ - $2.17$ eV ( $\sim 750$ nm to  $571$ nm) and orange-red emission,  $V_O$  : green emission  $\sim 2.17$ - $2.50$  eV ( $\sim 570$  nm to  $\sim 496$ nm] [Figure 6(c)].

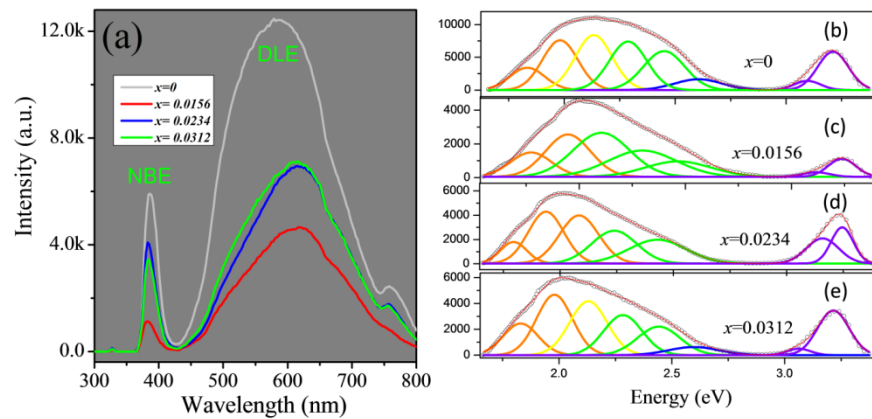


Figure 4.6 (a) Photoluminescence spectra consists of NBE and DLE regions of  $Zn_{(1-x)}(GaSi)_{x/2}O$  ( $x=0, 0.0156, 0.0234, 0.0312$ ); (b, c, d, e) deconvoluted PL spectral intensity vs energy of all samples

The PL spectra reveal a decrease of both the NBE and DLE peak intensities in the substituted samples than Z0. However, ZSGO1 is the least intense. The intensity increases with increasing substitution. However, the intensity for all the modified samples remained lower than the pristine ZnO [Figure 4.6(a)]. A Voigt function was applied to deconvolution the peaks of DLE and NBE regions [Figure 4.6(b, c, d, and e)]. The total color contribution was obtained for all samples by adding the individual areas obtained from the deconvolution of DLE and NBE regions [Figure 4.7(a)]. It was observed that  $V_O$  (green) decreased for ZSGO1, ZSGO2, but increased for ZSGO3.  $O_i$  defects (yellow) decreased for ZSGO1 but nominally increased for ZSGO2 and ZSGO3. Similarly,  $O_i$  related to orange-red emission decreased for ZSGO1 but increased considerably for ZSGO2 and ZSGO3 samples. This is a significant point as it relates the role of extra charge of both  $Si^{4+}$  and  $Ga^{3+}$  on the  $O_i$  population and simultaneous decrease of  $V_O$ . There were no changes observed for  $V_{Zn}$  (blue) and  $Zn_i$  (violet) in ZSGO samples.

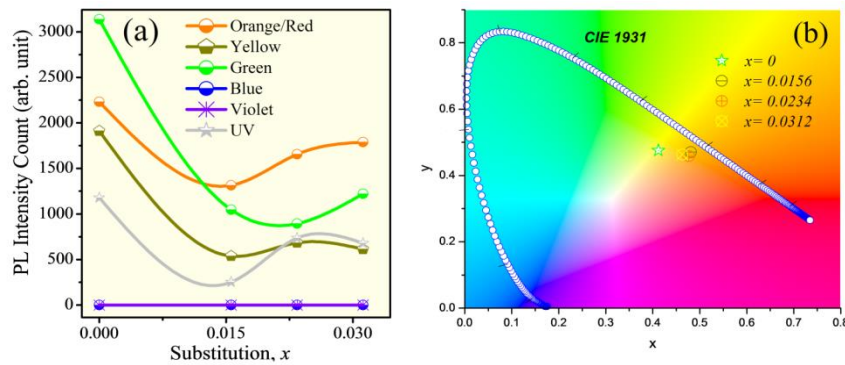


Figure 4.7(a) Deconvoluted PL intensity area count vs substitution  $x$  indicating variation in native defects of samples:  $Zn_{(1-x)}(GaSi)_{x/2}O$  ( $x=0, 0.0156, 0.0234, 0.0312$ ); (b) CIE plot of all samples (c) pictorial representation of energy level diagram showing native defects (in terms of wavelengths range) for all samples

*Commission Internationale de l'Elclairage (CIE)* plots was estimated to define the variation in color coordinate space [Figure 4.7(b)]. A significant variation was observed from a predominant yellowish-green

emission to a yellow-orange and orange-red emission. The orange red-shift further adds strengthens the claim of increased oxygen content in the lattice with an increase in  $\text{Ga}^{3+}/\text{Si}^{4+}$  concentration. These analyses from intensity and CIE support each other. The NBE region was examined and the nominal shifting in the samples towards higher energy with increasing substitution supports the results of Eg.

## Chapter 5

# Electrical properties of pure and doped ZnO

---

The electrical properties of ZnO and those modified by Ga and G-Si co-doping were studied by taking I-V measurements using Keithley sourcemeter 2450 and its carrier concentration and mobility measurements were determined using hall measurements. The doping has had profound effect on the electrical properties of ZnO and these changes have been explained with relation to valency and size of the dopant and the defect modification as discussed in the previous chapter.

### 5.1 Ga doped ZnO

#### 5.1.1 I-V measurements

The resistances of the samples were of the order of a few kilo-ohms and hence are few orders higher than junction resistances of the measurement circuit. This enabled estimation of conductivity,  $\sigma$ , for all samples in capacitance mode from Current-Voltage (I-V) measurements in the range 0 to 10V. I-V data revealed rise of current nearly proportionate with voltage implying a near metallic behavior [Figure 5.1(a)]. Conductivity,  $\sigma$ , was calculated for all samples. Increase of  $\sigma$  was observed from  $6 \times 10^{-9}$  S/cm in Z0 to  $1 \times 10^{-6}$  S/cm in ZG1. The value of  $\sigma$  continued to increase to  $1.45 \times 10^{-6}$  S/cm in ZG3. Thereafter,  $\sigma$  increased drastically by nearly one order to  $1.26 \times 10^{-5}$  S/cm in ZG4 [Figure 5.1(b)]. As Ga-content increases, an increase in the nature of conductivity is observed. This may be due to the extra charge available in  $\text{Ga}^{3+}$  than the parent  $\text{Zn}^{2+}$  ion in the lattice. Both  $\text{Zn}^{2+}$  and  $\text{Ga}^{3+}$  are neighboring atoms in the periodic table and have a complete  $3d^{10}$  orbital. Hence, the  $\text{Ga}^{3+}$  states are centers of extra charge carriers which are likely to contribute to the increased conductance of the materials.

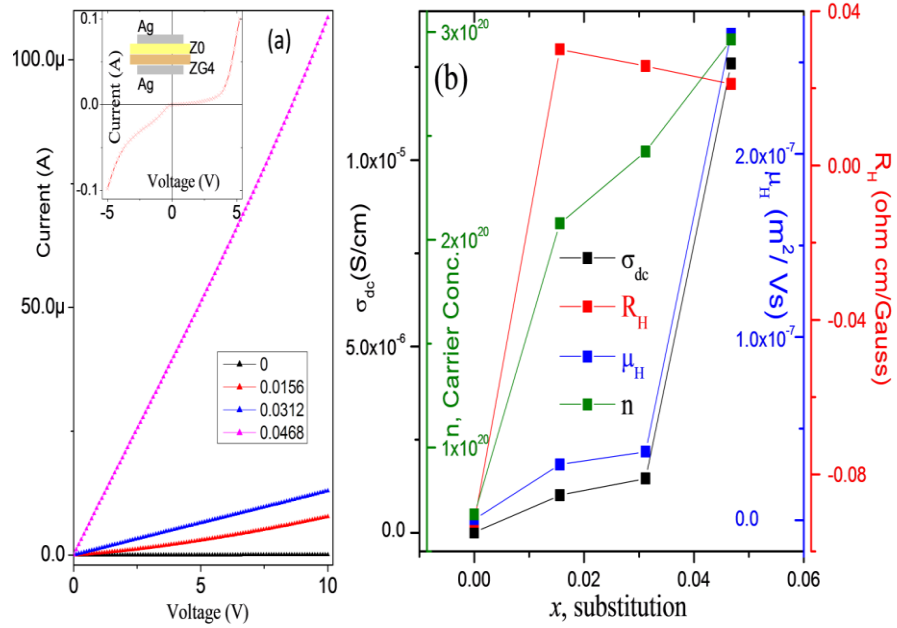


Figure 5.1 (a) Increase of conductivity with increasing substitution in the regime 0-10V; inset: P-N type diode behavior of double layer pellets of ZG0 and ZG4) (b) Increase of carrier concentration (n), conductivity ( $\sigma_{dc}$ ) and mobility ( $\mu_H$ ) with substitution; A negative Hall coefficient ( $R_H$ ) in parent ZnO (n-type semiconductor) changes sign to positive (p-type) with nominal introduction of Ga which thereafter remains positive but decreases with further substitution

### 5.1.2 Carrier properties (Hall effect measurements)

The nature of the charge carriers were estimated by Hall Effect measurements. Hall coefficient was calculated using the formula,  $R_H = V_H \cdot t / I_H \cdot B$  for different  $B$  values, where,  $V_H$  is the Hall voltage,  $I_H$  is the Hall current,  $t$  is the thickness of the pellet and  $B$  is the applied magnetic field. Values of  $R_H$  remained invariant with  $B$ . It is interesting to note that while pure ZnO showed negative  $R_H$  value of -0.092 ohm-cm/Gauss indicating an n-type material, the same were all positive for Ga-incorporated samples indicating a p-type semiconductor material. With  $Ga^{3+}$  doping in ZnO, the  $Zn^{2+}$  ions are replaced by  $Ga^{3+}$ . The extra charge of the dopant ion reduces the oxygen vacancies and creates O interstitial ions. From Photoluminescence CIE graph as

discussed in the previous chapter this is confirmed from the fact that the spectrum moves towards orange-red emission. These  $O_i$  defects are acceptor type and hence lead to transforming an n-type ZnO to a p-type Ga-doped ZnO [65–69]. The  $R_H$  value reduced with increasing Ga-content but remained positive. For ZG1 a value of 0.03 ohm-cm/Gauss was recorded while it reduced to 0.026 ohm-cm/Gauss for ZG3 and 0.021 ohm-cm/Gauss for ZG4 [Figure 5.1(b)]. These results are extremely exciting hinting at a p-type [29,69–77] semi-conduction in these Ga-substituted ZnO and hence repeated measurements were performed on these samples to verify these results. The decreases nature of  $R_H$  for the substituted samples is due to the increasing carrier concentration with Ga-incorporation. To further verify the n-type nature of Z0 and p-type nature of the ZG4 samples, a double layer pellet was pressed at 2 kPa and sintered at 600°C for 2 hours with Z0 in one side and ZG4 on the other. Silver paste electrodes were painted and cured on both sides in capacitance mode. The resultant device showed a diode-like behavior [Figure 5.1(a) inset] confirming the n-type and p-type nature of the materials.

The carrier concentration of the samples were calculated using the equation  $n = 1 / (R_H \cdot q)$ , where  $q$  is the electronic charge. A dramatic increase was observed for  $n$  from  $6.8 \times 10^{19}/\text{c.c.}$  in Z0 to  $2.1 \times 10^{20}/\text{c.c.}$  in ZG1 and thereafter it increases linearly to  $2.42 \times 10^{20}/\text{c.c.}$  in ZG3 to  $\sim 3 \times 10^{20}/\text{c.c.}$  in ZG4 [Figure 5.1(b)]. On the other hand the mobility of the charge carriers also improved drastically from  $5.55 \times 10^{-10} \text{ cm}^2/\text{Vs}$  in Z0 to  $3 \times 10^{-8} \text{ cm}^2/\text{Vs}$  in ZG1. With further increase in substitution mobility increased to  $3.75 \times 10^{-8} \text{ cm}^2/\text{Vs}$  in ZG3 to  $2.66 \times 10^{-7} \text{ cm}^2/\text{Vs}$  in ZG4 as shown in [Figure 9(b)]. Thus with increased mobility and number of charge carriers, ZG samples are good candidates for electronic devices [78–80] with lesser amount of defect states and a more perfect lattice.

## 5.2 Electrical properties of Ga-Si doped ZnO

### 5.2.1 I-V measurement

The current vs voltage characteristics reveal nearly linear dependence of current with voltage which is an indication of ohmic behavior. Voltage dependence on current was obtained from current-voltage (I-V) characteristics [Figure 5.2(a)]. Current for the co-doped sample increases exponentially to  $\sim 10^2$  times. Conductivity is primarily dependent on carrier concentration and carrier mobility [21,38,76]. The donor concentration in the ZnO lattice increases due to the higher charges of  $\text{Si}^{4+}$  and  $\text{Ga}^{3+}$  which increases the carrier concentration. Due to decrease in oxygen related defects and an increase in the regularity of the lattice, electrons are less scattered as confirmed by Urbach energy study. These modifications in the ZnO lattice could well lead to enhanced conductivity. Hence, an explanation in the light of a Burstein-Moss shift seems logical. I-V studies reveal an increase of conductance with substitution [Figure 5.2(b)].

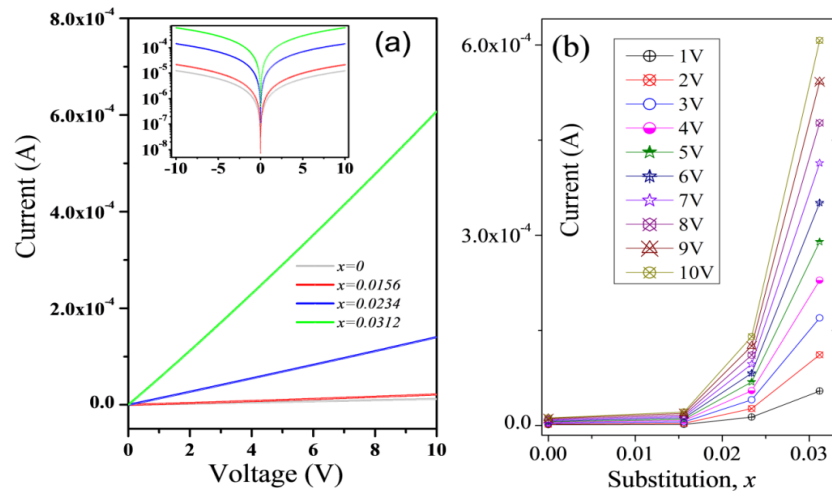


Figure 5.2 (a) I-V plot with substitution  $x$  of samples (inset; the logarithmic plot of current vs voltage), (b) plot for current variation with composition for different voltage

In connection to the discussion on  $\text{Zn}_\text{O}$  and  $\text{O}_\text{Zn}$  antisites in the PL section in the previous chapter, it is important to point out that these

antisites are also responsible for the enhancement of conductive properties. In agreement with the suggestions made in defect studies, the conductive properties hence are supportive evidence.

### 5.2.2 Carrier Properties (Hall Effect measurement)

The nature of the charge carriers was estimated by Hall Effect measurements. Hall coefficient was calculated using the formula,  $R_H = V_H \cdot t / I_H \cdot B$  for different B values, where,  $V_H$  is the Hall voltage,  $I_H$  is the Hall current,  $t$  is the thickness of the pellet and  $B$  is the applied magnetic field.  $R_H$  remained negative and invariant with applied field,  $B$ . This ensures n-type conduction. However,  $R_H$  reduced with increasing GaSi-content: 0.17, 0.078, 0.022 and 0.014 (in units of ohm-cm/Gauss) for Z0, ZSGO1, ZSGO2 and ZSGO3 respectively [Figure 8]. This decreasing nature of  $R_H$  with Ga-substitution is due to the increasing carrier concentration,  $n$ , where,  $n = 1 / (R_H \cdot q)$  and  $q$  is the electronic charge. The values of  $n$  for the Z0, ZSGO1, ZSGO2 and ZSGO3 samples were recorded as 3.70, 7.9, 29.0 and 46.1 (in units of  $10^{19}/\text{c.c.}$ ) respectively [Figure 5.3]. The increasing carrier concentration is also indicative of defect levels created in the CB, as discussed in previous sections.

The order of the resistances ( $R$ ) was of a few kilo-ohms whereas the junction resistances are generally a few ohms. Hence, the linear nature of the I-V characteristics can be attributed to the Ohmic nature of the samples. The electrode separation,  $L$ , and cross sectional area,  $A$ , were measured and the conductivity,  $\sigma$ , was calculated using the formula:  $\sigma = L/RA$ . The  $\sigma$  values of 7.69, 17.5, 260 and 430 (in units of  $10^{-6} \text{ S/cm}$ ) were observed for Z0, ZSGO1, ZSGO2 and ZSGO3 respectively [Figure 5.3]. This increasing nature of conductivity may arise from the extra charge of  $\text{Ga}^{3+}$  and  $\text{Si}^{4+}$  than the parent  $\text{Zn}^{2+}$  ion, and falls in line with the I-V studies.

On the other hand the mobility,  $\mu$ , of the charge carriers was calculated using the formula:  $\mu = R_H \cdot \sigma$ . It is to be noted that the  $\mu$  values although increased with substitution, did not change orders with substitution.

For Z0, ZSGO1, ZSGO2 and ZSGO3 samples,  $\mu$  values of 1.3, 1.38, 5.61, 5.83 (in units of  $\text{cm}^2/\text{Vs}$ ) were observed respectively [Figure 5.3]. Hence, the conductivity rises due to increase of carrier concentration as well as the mobility factor due to lesser defect states in the doped samples.

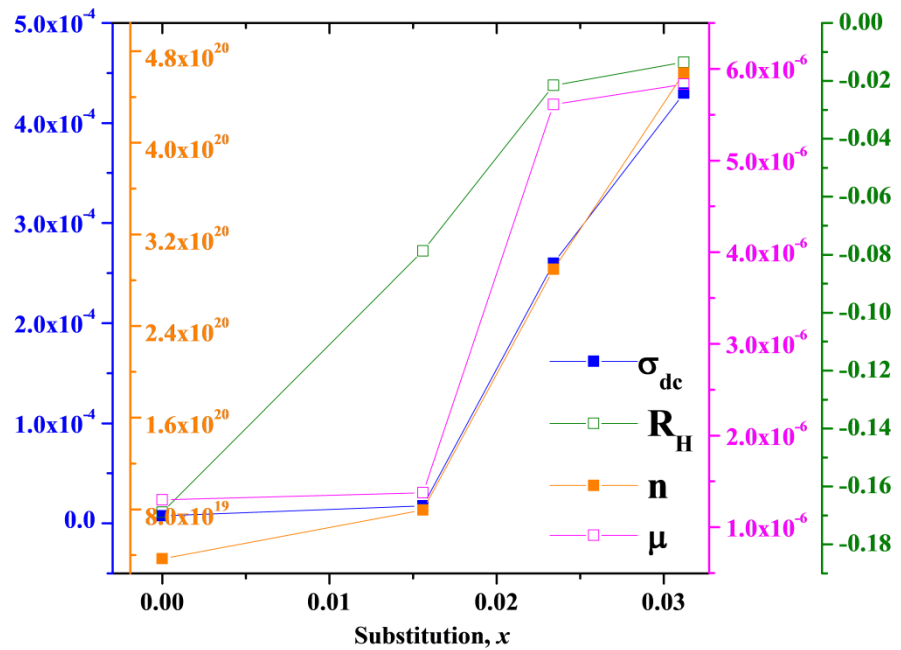


Figure 5.3 Increase of carrier concentration ( $n$ ), conductivity ( $\sigma_{dc}$ ) and mobility ( $\mu$ ) with substitution; A negative Hall coefficient ( $R_H$ ) (n-type semiconductor) in  $\text{Zn}_{(1-x)}(\text{GaSi})_{x/2}\text{O}$  ( $x=0, 0.0156, 0.0234, 0.0312$ )

Note that local defect states of either donor or acceptor types are instrumental in increasing the mobility of charge carriers. Hence, conduction increase is most likely due to an accumulated result of defect states available inside the CB due to excess oxygen related defects as discussed in the PL section.

## Chapter 6

# UV and Visible light sensing properties of pure and doped ZnO

---

Ultraviolet detection has become an important aspects of science and technology related with health, environment and even space research[117,118T]. UV detectors based on silicon although available in the market are not cost efficient as they require expensive visible light filters. Faster, more sensitive, cost-effective UV detection is therefore an important research area. ZnO is easily available, cost efficient, non-toxic, does not pose a threat to the environment and has good thermal and chemical stability with high photoconductivity.

Visible light sensing can be an indispensable tool for mankind with possible applications in communication, traffic safety and automated robots. ZnO has defect levels in the band gap which can be modified by doping and changing the synthesis conditions. This modification allows for customized properties. One of the property worth exploring is the visible light sensing property of ZnO. Light in the visible region does not have good sensitivity for pure ZnO however by modifying the defect levels UV sensitivity can be suppressed and the sensitivity to a particular colour of light enhanced. In this thesis we show enhanced red light sensing with suppressed UV sensing in co-doped samples. Pure ZnO nanoparticles normally show a relatively poor UV sensing. This is due to large n-type carrier concentration as well as fast recombination rate of photoexcited electron–hole pairs. To resolve this fundamental issue, defect engineering and doping processes have been applied to tailor certain properties of ZnO.

### 6.1 UV sensing property of Ga doped ZnO

A in house build UV to Visible light sensing setup was used to study the sensing properties of the samples. With 8V bias the current between electrodes enhances upon UV illumination and decreases when the UV light is turned off [Figure 6.1(a)]. Repeated cycles of ON

and OFF in intervals of 7min have been recorded for all the samples. Four such cycles are shown [Figure 6.1(a)]. Current increases with UV illumination, to a maximum,  $I_{UV\_max}$ , and decreases similarly, after the light was turned off, to a minimum in darkness,  $I_{dark\_min}$  [Figure 6.1(a)].  $I_{dark\_min}$  follows a similar trend of current from the I-V characteristics and increases drastically with minimum Gallium incorporation and thereafter increasing further with higher substitution [Figure 6.1(a)]. This implies an increase of conductance in the presence of Ga in the lattice.

The sensing photocurrent ( $\Delta I$ ), can be estimated from the difference between  $I_{UV\_max}$  and  $I_{dark\_min}$ ; i.e.  $\Delta I = I_{UV\_max} - I_{dark\_min}$  which increases with Ga-addition. Sensitivity,  $S$ , of samples may be defined as  $S = (\Delta I/I_{dark\_min}) * 100$ .  $\Delta I$  increase at a lesser rate than  $I_{dark\_min}$  [Figure 6.1(b)]. Hence, the overall  $S$  decreases with an increase in  $Ga^{3+}$  doping [Figure 6.1(c)].

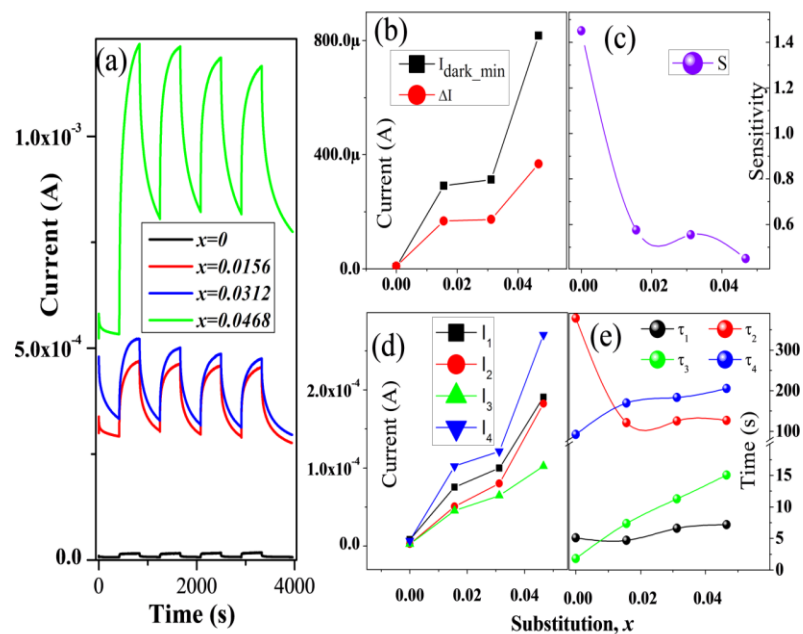


Figure 6.1(a) Dynamic changes in current for different  $x$  (b, c) increase in  $\Delta I$  and  $I_{dark\_min}$  and decrease in sensitivity with increasing substitution (d) increasing trend of growth and decay currents with substitution (e) fast and slow response and recovery times with substitution  $x$

The basic mechanism of UV sensing can be explained on the basis of adsorption and desorption of oxygen molecules from the surface of samples. With UV illumination, photo-generated electron-hole pairs are produced on the surface of the pellets:  $h\nu \rightarrow e^- + h^+$ , where,  $h\nu$  is photon energy,  $h^+$  and  $e^-$  are photo-generated hole in the valence band and electron in the conduction band, respectively. The photo-generated holes in valence band recombine with adsorbed oxygen ions on the surface, producing an oxygen molecule. This process is described as:  $h^+ + O_2^-(ad) \rightarrow O_2$ . Simultaneously, desorption of oxygen ions adsorbed onto the surface and produces photo-generated electrons [13]:  $O_2^- \rightarrow O_2 + e^-$ . However, from the formula of sensitivity, it seems that sensitivity is strongly dependent on  $I_{dark\_min}$ . In spite of sensitivity being lowered with Ga-doping, the sensing photocurrent ( $\Delta I$ ) increases.

The response and recovery of the UV sensing process follows an exponential nature [Figure 6.1(a)]. A single exponential formula seems difficult to address the issue. Hence, a bi-exponential formula for the current,  $I_g = I_{g0} + I_1 \exp(-\tau/\tau_1) + I_2 \exp(-\tau/\tau_2)$  was fitted to both growth of current, where  $I_{g0}$  is the current offset;  $I_1, I_2$  are positive constants. Similarly,  $I_d = I_{d0} + I_3 \exp(-\tau/\tau_3) + I_4 \exp(-\tau/\tau_4)$  was used for current decay. In the response graph  $\tau_1$  is smaller than  $\tau_2$ , thereby representing a faster process. Similarly, the recovery process has a similar faster process represented by the decay time  $\tau_3$  and a slower process represented by  $\tau_4$ .

Note that both processes become slower with substitution in case of response mechanism. However with substitution the slower recovery process becomes faster while the faster one becomes slower [Figure 6.1(e)]. The speed of the processes may be correlated with oxygen-related defects of the system as with substitution the defect densities vary in a similar trend. It is observed that, for ZG3 and ZG4 samples yellow emission increases. Most probably speed of response or recovery is due to  $O_i$  defects. It is interesting to note that the two

processes for the response mechanism are comparable in terms of current in Figure 6.1(d), whereas the faster process is much weaker than the slower process for the response mechanism [Figure 6.1(e)]. However, the compositional dependence of these current contributions resembles the trend of carrier concentration, thereby hinting at a direct correlation between the two.

## 6.2 UV and Visible light sensing in Ga-Si doped ZnO

Using a homemade setup photo-sensing properties of all samples were studied for four different wavelengths in the UV to the visible region: UV (290nm), blue (450nm), green (540nm) and red (640nm). For all the four different light sources, an exponential rise followed by an exponential fall of current is observed with the illumination of light followed by darkness respectively. A general equation was accepted for both the growth and decay of current of the form:  $I = I_0 + I_1 \exp(-\tau/\tau_1) + I_2 \exp(-\tau/\tau_2)$ ; [13,45,66,77] with two time-constants,  $\tau_1$ ,  $\tau_2$ , and three characteristic currents  $I_0$ ,  $I_1$ ,  $I_2$ . It is interesting to note that in both the growth and decay of current, there is a fast and a slow process involved with two different current components. The current components change with the illumination color as shown in [Figure 9(a, b, c, d)]. From the values of these current components, an attempt to find the actual current in darkness and in the specific light illumination has been discussed. For a current growth mechanism, the current can be written as:  $I = I_0(\text{max}) - I_{g1} \exp(-\tau/\tau_{g1}) - I_{g2} \exp(-\tau/\tau_{g2})$ , while for the decay:  $I = I_0(\text{min}) + I_{d1} \exp(-\tau/\tau_{d1}) + I_{d2} \exp(-\tau/\tau_{d2})$ . Hence, the estimated current in darkness,  $I_{\text{min}}$ , can be estimated as either,  $I_0(\text{max}) - I_{g1} - I_{g2}$ , or,  $I_0(\text{min})$ , while the maximum current in the presence of the light can be estimated as either  $I_0(\text{min}) + I_{d1} + I_{d2}$ , or  $I_0(\text{max})$ . Depending on the fastness of the two decay processes of excitation, the response behavior shows a stable or increasing tendency. The sensitivity,  $S = (\Delta I/I_{\text{min}}) * 100$ ,<sup>9,10,47,78</sup> was calculated [Figure 11(a, b)] for all the samples, for all colors, where, the sensing photocurrent,  $\Delta I = I_{\text{max}} - I_{\text{min}}$ .

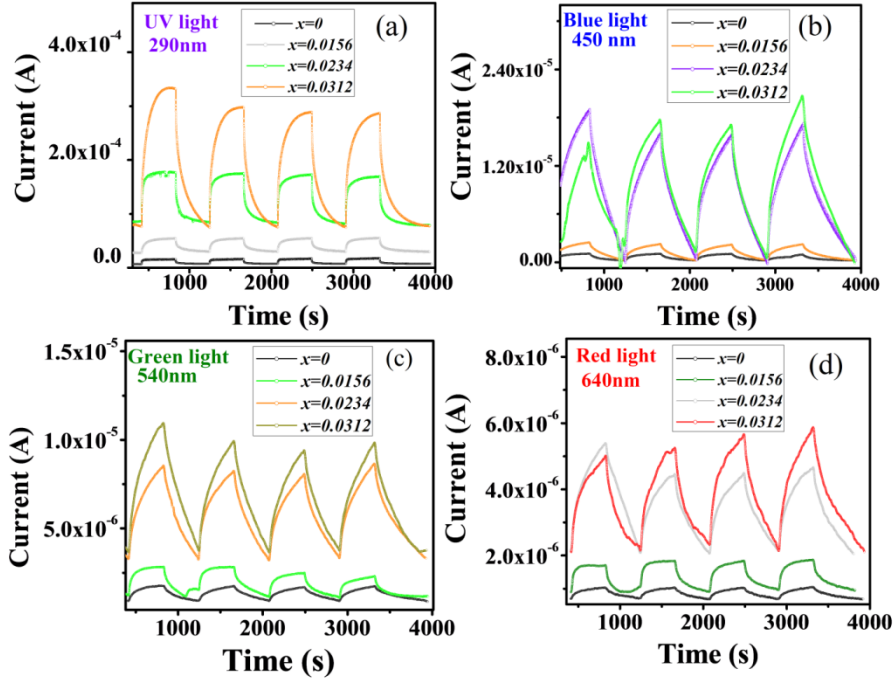


Figure 6.2(a, b, c, d) Variation in current w.r.t. time for different substitution  $x$ , under UV and visible lights (290nm, 450nm, 540nm, 640nm) irradiation

In the absence of UV light, oxygen molecules get adsorbed on the surface as negatively charged ions. The free electrons available in the conduction band are available for a process that leads to adsorption of an environmental O ion  $h^+ (hv) + O^{2-} \text{ adsorbed} \rightarrow O^2 (g), O^2 (g) + e^- \rightarrow O^{2-} \text{ adsorbed}$ [7,13,78,79]. This adsorbed O creates a depletion layer with low conductivity at the surface. With UV-illumination, a photon with energy more than the  $E_g$  generates an electron-hole pair. The adsorbed oxygen ions combine with the holes to produce oxygen molecules: where,  $h\nu$  is the photon energy,  $h^+$  and  $e^-$  is the photo-generated holes and electrons respectively. Hence the adsorbed O ion is desorbed from the surface.

A similar process of O adsorption and desorption can be formulated for visible light illumination. It has been discussed that the defect states owing to  $V_O, O_i, V_{Zn},$  and  $Zn_i$  vary from sample to sample depending on the amount of substitution. The electrons available in these defects are in metastable states and often lead to different decay mechanisms.

The response to these different lights, therefore, varies with firstly the population density of these defect states and their transition probabilities to either the valence band or the conduction band. The creation and annihilation of electron-hole pairs, therefore, depend on these properties and thereby changes the response behavior of the samples.

## **6.2 UV and Visible Light sensing Ga-Si co-doped ZnO**

### **6.2.1 UV-Sensing: Response:**

The faster response time-constant,  $tg_1$  increases nominally for ZSGO1 and thereafter decreases for further substitution. On the other hand the slower time-constant  $tg_2$  becomes faster than the undoped sample and continues to become faster with increasing substitution [Figure 10(b2)]. The current components of both slower and faster processes for the response/growth process increases with increasing substitution. The current components of the slower and faster processes for a specific sample are comparable [Figure 10(b1)]. Hence, the Ga-Si substitution helps in achieving a faster UV-sensing mechanism.

**Recovery:** For the decay process the faster time-constant  $td_1$  increases considerably with substitution, while the slower time-constant  $td_2$  increases nominally [Figure 10(b2)]. Hence, the reverse scenario is observed between growth and decay of the currents [Figure 10(b1)]. This is an indication of delayed transitions from intrinsic defect states to the valence band. This should have an impact on the current and the background current,  $I_{min}$ , is supposed to increase with time as the excited electrons are trapped in some of these defects. It appears that with increasing substitutional centers the electrons ease in transiting to an excited state but are lazy to return back to the ground state.

### **6.2.2 Blue-light Sensing:**

**Response:** It is observed that the fast response time-constant  $tg_1$  nominally increases for ZSGO1, i.e. the process becomes slower. However, for further substitution the process starts to be faster and

becomes fastest for ZSGO3. However, the slower response time-constant  $tg_2$  nominally decreases for ZSGO1 but thereafter increases with substitution [Figure 6.3(c2)]. It is interesting to note that the current component of the slower process becomes stronger than the faster component with substitution [Figure 6.3(c1)]. Hence, with substitution blue-light-response becomes slower.

**Recovery:** The faster recovery time-constant,  $td_1$ . Initially becomes slower in ZSGO1 than Z0. It is even slower in ZSGO2 than ZSGO1 but thereafter becomes faster for ZSGO3. The slower recovery time-constant,  $td_2$  has a similar trend as slower response time-constant,  $tg_2$ , [Figure 6.3(c2)]. This may be related to the introduction of defects which can trap and also release electrons at a slower rate. The current associated with the slower process is much higher than the faster process and increases with substitution [Figure 6.3(c1)]. The response is generally faster than recovery. Hence, accumulation of trapped charges in defect states happens in the case of blue-light sensing similar to UV sensing.

### 6.2.3 Green-light Sensing:

The green-light sensing parameters are similar to the blue-light sensing parameters and show an equivalent trend except for the trend in the faster response and recovery process time-constants [Figure 6.3(d1, d2)].

### 6.2.4 Red-light Sensing:

**Response:** The fast and slow growth processes of red-light response ( $tg_1$ ,  $tg_2$ ) have equivalent current components in contrast to green-light response [Figure 6.3(e1, e2)]. The increase and decrease of the growth time-constants although time in values, follow a similar trend and also bears a close similarity with the green light sensing.

**Recovery:** The recovery current is similar to the growth current in magnitude as well as the trend of increasing nature with substitution. Both the fast and slow recovery time-constants  $td_1$  and  $td_2$  show an

increasing trend [Figure 6.3(e1)]. This is not similar to the trend of the growth currents and the values of the decay constants are lesser than the growth constants [Figure 6.3(e2)]. The difference in these growth and decay time-constants indicate that the decay happens faster than the growth hence charge accumulation is reduced.

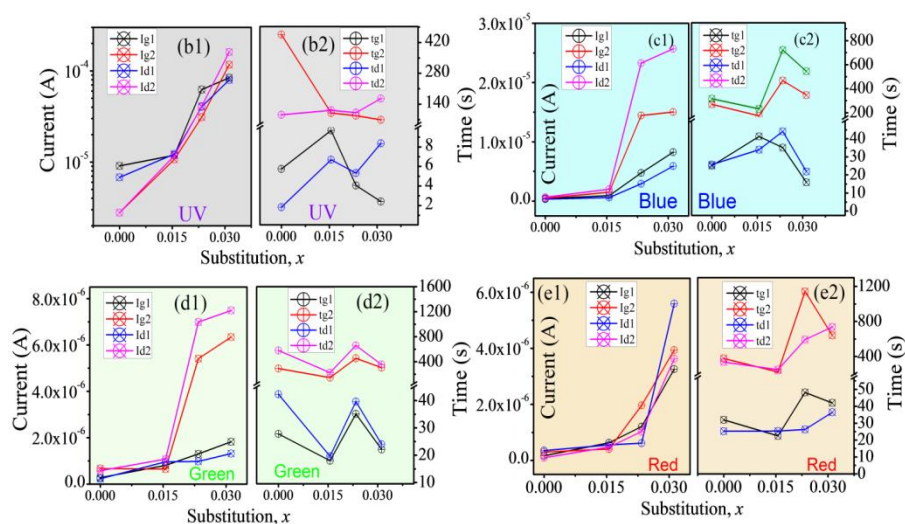


Figure 6.3 (b1, c1, d1, e1) shows trend of growth and decay currents vs substitution  $x$ , (b2, c2, d2, e2) shows variation of fast and slow response and recovery times vs substitution  $x$  respectively for  $\text{Zn}_{(1-x)}(\text{GaSi})_{x/2}\text{O}$  ( $x=0, 0.0156, 0.0234, 0.0312$ )

### 6.2.4 Photocurrent and Sensitivity:

The sensing photocurrent ( $\Delta I$ ), is the difference between  $I_{\max}$  and  $I_{\min}$ ; i.e.  $\Delta I = I_{\max} - I_{\min}$ .  $\Delta I$  increases with substitution. However, the calculation of sensitivity,  $S$ , which is actually an estimation of percentage increase of  $\Delta I$  w.r.t. the dark current, shows a different trend [Figure 6.4(a, b)].

For UV-light sensitivity decreases with increase of substitution, but for all other lights, the sensitivity increases. Hence, while the pure ZnO sample is a good UV-sensing material, other color-sensing deteriorates with increasing wavelength. The ZSGO1 and ZSGO2 are most sensitive to blue, green lights. However, ZSGO3 is most sensitive to

red-light. Hence, ZSGO3 material can be a very efficient red-light sensor.

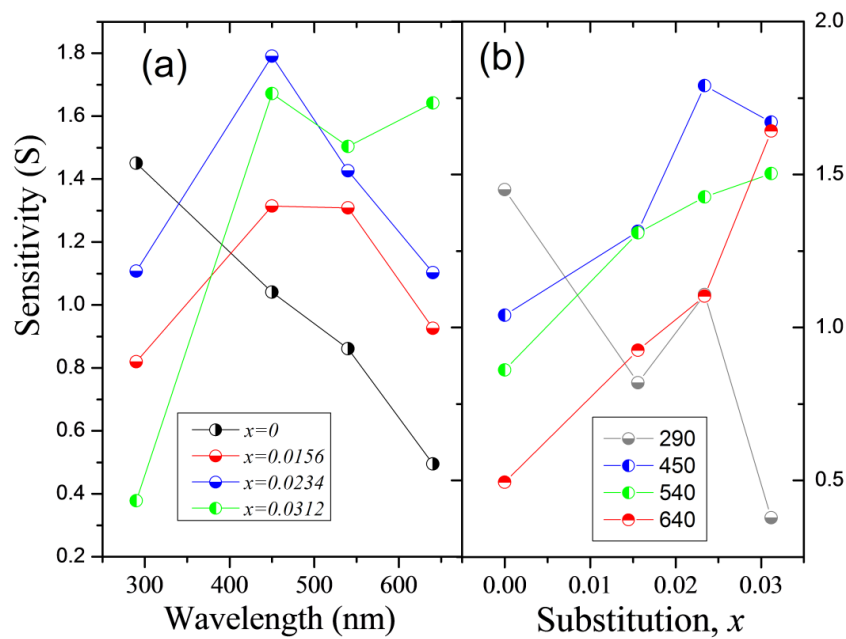


Figure 6.4 (a) variation of sensitivity with Wavelength of Zn<sub>(1-x)</sub>(GaSi)<sub>x</sub>/2O ( $x=0, 0.0156, 0.0234, 0.0312$ ) ; (b) sensitivity variation with substitution  $x$  for different wavelengths (290, 450, 540 and 640)nm

The extra charge of  $Si^{4+}/Ga^{3+}$  changes the  $O_i$  and  $V_O$  population. This is observed from the CIE plot. The trend of changes in sensitivity for different colored-lights also follows the same trend as the changes in defects with substitution. Hence, sensitivity may be a direct coincidence of these defect populations.

## Chapter 7

### Conclusion and Future Scope

---

Single phase, wurtzite  $Zn_{1-x}Ga_xO$  ( $x= 0, 0.0156, 0.0312$  and  $0.0468$ ) samples were synthesized using sol-gel method. Ga substitution leads to nominal changes in lattice parameters with a significant increase in  $E_g$  from 3.21 eV to 3.28 eV. Ga doping helps in reducing defects and improving regularity of lattice. The extra charge of  $Ga^{3+}$  invites more carriers. Ga-incorporation also helps improve the mobility of the carriers. Interestingly, the Hall voltage changes polarity from negative in pure ZnO to positive in Ga-substituted samples, implying p-type semi-conduction. The carrier concentration and mobility shows drastic improvement with substitution making this material also an ideal candidate for a TCO. Although the promptness of the UV-sensing mechanism is reduced in Ga-substituted samples the sensing current is enhanced. The promptness of response and recovery has been related to the amount of oxygen interstitials and latent defects. Increase of photocurrent is proportionately lesser than the increase of dark current. Hence, dark current is a dominant factor in the estimation of UV sensitivity in the materials.

$Ga^{3+}/Si^{4+}$  co-doping in ZnO reveals a *wurtzite* structured solid solution. No extra unknown phonon modes were detected in Raman spectroscopy. The absence of any other element other than adventitious carbon certifies the chemical purity of the samples without the presence of impurities due to N and H. The structural and vibrational studies confirm the improvement of crystallinity of the samples with increasing substitution. Increase in bandgap with decreasing lattice strain is obtained with increasing substitution. PL spectra reveal a decrease of both the NBE and DLE peak intensities in the substituted samples than Z0. However, both features intensify in ZSGO3 as compared to ZSGO1 and ZSGO2 but are less intense than Z0. Hence, surface defects reduces with substitution until ZSGO2 but enhances for

ZSGO3. The CIE plot shows the orange-red shift supporting a reduction in  $V_O$ . Hall coefficient,  $R_H$  remained negative and invariant with applied field ensuring n-type conduction but reduced with increasing GaSi-content. The conductivity rises due to increase of carrier concentration as well as the mobility factor due to lesser defect states in the doped samples. Note that local defect states of either donor or acceptor types are instrumental in increasing the mobility of charge carriers. Hence, conduction increase is most likely due to an accumulated result of defect states available inside the CB due to excess oxygen related defects as discussed in the PL section.

The photocurrent and photo-sensitivity for illumination of different wavelengths of light from UV (290nm) to visible range (450nm, 540nm, 640nm) were tested on sol-gel processed  $Zn_{1-x}(SiGa)_x/2O$ . Photocurrent increases with substitution. The pure ZnO sample is a good UV-sensing material.

In pure ZnO other light sensing deteriorates with increasing wavelengths. In contrast for ZSGO3, sensitivity increased continuously from UV to red-light sensing. Thus, while Z0 is a good UV sensitive material, ZSGO3 is a good red-light sensitive material. The trend of changes in sensitivity for different substitutions also follows a similar trend as the changes in defects with substitution. Hence sensitivity may be a direct consequence of these defect populations.

### **Future scope**

During the course of this thesis we have studied the effect of doping gallium and codoping gallium and silicon primarily on the defect states and optical band gap and structural properties. The temperature chosen for annealing was 600°C. This has shown promises for applications of the material as a TCO and as a sensing material for Red Light. Different doping elements and co-doping may lead to other exciting results. The magnetic and dielectric properties of the material can be tailored by doping with suitable elements. With suitable dopants ZnO might find applications in gas sensing and also for thermoelectric energy

generation. A change in the annealing temperature and atmospheric conditions of annealing may also lead to interesting results and possibly properties with good applicability.

## REFERENCES

- [1] H. Zhang, J. Feng, J. Wang, M. Zhang, Preparation of ZnO nanorods through wet chemical method, *Mater. Lett.- MATER LETT.* 61 (2007).
- [2] V.A. Coleman, C. Jagadish, Chapter 1 - Basic Properties and Applications of ZnO, in: *Zinc Oxide Bulk Thin Films Nanostructures*, Elsevier Science Ltd, Oxford, 2006: pp. 1–20. doi:10.1016/B978-008044722-3/50001-4.
- [3] Z.L. Wang, Zinc oxide nanostructures: growth, properties and applications, *J. Phys. Condens. Matter.* 16 (2004) R829. doi:10.1088/0953-8984/16/25/R01.
- [4] A. Mang, K. Reimann, S. Rübenacke, Band gaps, crystal-field splitting, spin-orbit coupling, and exciton binding energies in ZnO under hydrostatic pressure, *Solid State Commun.* 94 (1995) 251–254. doi:10.1016/0038-1098(95)00054-2.
- [5] D.C. Look, Recent advances in ZnO materials and devices, *Mater. Sci. Eng. B.* 80 (2001) 383–387. doi:10.1016/S0921-5107(00)00604-8.
- [6] Ü. Özgür, Y.I. Alivov, C. Liu, A. Teke, M.A. Reshchikov, S. Doğan, V. Avrutin, S.-J. Cho, H. Morkoç, A comprehensive review of ZnO materials and devices, *J. Appl. Phys.* 98 (2005) 041301. doi:10.1063/1.1992666.
- [7] N.H. Nickel, E. Terukov, *Zinc Oxide - A Material for Micro- and Optoelectronic Applications: Proceedings of the NATO Advanced Research Workshop on Zinc Oxide as a Material for Micro- and Optoelectronic Applications*, held in St. Petersburg, Russia, from 23 to 25 June 2004, Springer Science & Business Media, 2006.
- [8] B.K. Meyer, H. Alves, D.M. Hofmann, W. Kriegseis, D. Forster, F. Bertram, J. Christen, A. Hoffmann, M. Straßburg, M.

- [9] Dworzak, U. Haboeck, A.V. Rodina, Bound exciton and donor–acceptor pair recombinations in ZnO, *Phys. Status Solidi B.* 241 (2004) 231–260. doi:10.1002/pssb.200301962.
- [10] F. Tuomisto, K. Saarinen, D.C. Look, G.C. Farlow, Introduction and recovery of point defects in electron-irradiated ZnO, *Phys. Rev. B.* 72 (2005) 085206. doi:10.1103/PhysRevB.72.085206.
- [11] D.C. Look, J.W. Hemsky, J.R. Sizelove, Residual Native Shallow Donor in ZnO, *Phys. Rev. Lett.* 82 (1999) 2552–2555. doi:10.1103/PhysRevLett.82.2552.
- [12] A. Janotti, C.G.V. de Walle, Fundamentals of zinc oxide as a semiconductor, *Rep. Prog. Phys.* 72 (2009) 126501. doi:10.1088/0034-4885/72/12/126501.
- [13] A. Janotti, C.G. Van de Walle, Native point defects in ZnO, *Phys. Rev. B.* 76 (2007) 165202. doi:10.1103/PhysRevB.76.165202.
- [14] T.T. Loan, N.N. Long, L.H. Ha, Photoluminescence properties of Codoped ZnO nanorods synthesized by hydrothermal method, *J. Phys. Appl. Phys.* 42 (2009) 065412. doi:10.1088/0022-3727/42/6/065412.
- [15] F.C. Romeiro, J.Z. Marinho, A.C. A. Silva, N.F. Cano, N.O. Dantas, R.C. Lima, Photoluminescence and Magnetism in Mn<sup>2+</sup>-Doped ZnO Nanostructures Grown Rapidly by the Microwave Hydrothermal
- [16] Method, *J. Phys. Chem. C.* 117 (2013) 26222–26227.

- [17] H. Zhu, J. Iqbal, H. Xu, D. Yu, Raman and photoluminescence properties of highly Cu doped ZnO nanowires fabricated by vaporliquid-solid process, *J. Chem. Phys.* 129 (2008) 124713. doi:10.1063/1.2981050.
- [18] A. Mang, K. Reimann, S. Rübénacke, Band gaps, crystal-field splitting, spin-orbit coupling, and exciton binding energies in ZnO under hydrostatic pressure, *Solid State Commun.* 94 (1995) 251–254. doi:10.1016/0038-1098(95)00054-2.
- [19] D.C. Look, Recent advances in ZnO materials and devices, *Mater. Sci. Eng. B.* 80 (2001) 383–387. doi:10.1016/S0921-5107(00)00604-8.
- [20] Ü. Özgür, Y.I. Alivov, C. Liu, A. Teke, M.A. Reshchikov, S. Doğan, V. Avrutin, S.-J. Cho, H. Morkoç, A comprehensive review of ZnO materials and devices, *J. Appl. Phys.* 98 (2005) 041301. doi:10.1063/1.1992666.
- [21] N.H. Nickel, E. Terukov, *Zinc Oxide - A Material for Micro- and Optoelectronic Applications: Proceedings of the NATO Advanced Research Workshop on Zinc Oxide as a Material for Micro- and Optoelectronic Applications, held in St. Petersburg, Russia, from 23 to 25 June 2004*, Springer Science & Business Media, 2006.
- [22] F. Tuomisto, K. Saarinen, D.C. Look, G.C. Farlow, Introduction and recovery of point defects in electron-irradiated ZnO, *Phys. Rev. B.* 72 (2005) 085206. doi:10.1103/PhysRevB.72.085206.
- [23] J. Song, Y. He, J. Chen, D. Zhu, Z. Pan, Y. Zhang, J. Wang, Bicolor

Light-Emitting Diode Based on Zinc Oxide Nanorod Arrays and Poly(2-methoxy,5-octoxy)-1,4-phenylenevinylene, *J. Electron. Mater.* 41 (2012) 431–436. doi:10.1007/s11664-011-1783-x.

[24] D. J. Rogers, F. Hosseini Teherani, V. E. Sandana, M. Razeghi, ZnO thin films and nanostructures for emerging optoelectronic applications, in: 2010: p. 76050K–7605–11. <http://dx.doi.org/10.1117/12.862634>.

[25] H. Zeng, X. Xu, Y. Bando, U.K. Gautam, T. Zhai, X. Fang, B. Liu, D. Golberg, Template Deformation-Tailored ZnO Nanorod/Nanowire Arrays: Full Growth Control and Optimization of Field-Emission, *Adv. Funct. Mater.* 19 (2009) 3165–3172. doi:10.1002/adfm.200900714.

[26] H. Zhang, J. Feng, J. Wang, M. Zhang, Preparation of ZnO nanorods through wet chemical method, *Mater. Lett. - MATER LETT.* 61 (2007) 5202–5205. doi:10.1016/j.matlet.2007.04.030.

[27] V.A. Coleman, C. Jagadish, Chapter 1 - Basic Properties and Applications of ZnO, in: *Zinc Oxide Bulk Thin Films Nanostructures*, Elsevier Science Ltd, Oxford, 2006: pp. 1–20. doi:10.1016/B978-008044722-3/50001-4.

[28] A. Stadler, Transparent Conducting Oxides-An Up-To-Date Overview, *Mater. Basel Switz.* 5 (2012) 661–683. doi:10.3390/ma5040661.

- [29] C.G. Granqvist, Transparent conductors as solar energy materials: A panoramic review, *Sol. Energy Mater. Sol. Cells*. 91 (2007) 1529–1598. doi:10.1016/j.solmat.2007.04.031.
- [30] T. Minami, Substitution of transparent conducting oxide thin films for indium tin oxide transparent electrode applications, *Thin Solid Films*. 516 (2008) 1314–1321. doi:10.1016/j.tsf.2007.03.082.
- [31] E. Monroy, F. Omnès, F. Calle, Wide-bandgap semiconductor ultraviolet photodetectors, *Semicond. Sci. Technol.* 18 (2003) R33. doi:10.1088/0268-1242/18/4/201.
- [32] K. Liu, M. Sakurai, M. Liao, M. Aono, Giant Improvement of the Performance of ZnO Nanowire Photodetectors by Au Nanoparticles, *J. Phys. Chem. C*. 114 (2010) 19835–19839. doi:10.1021/jp108320j.
- [33] A.J. Gimenez, J.M. Yáñez-Limón, J.M. Seminario, ZnO–Paper Based Photoconductive UV Sensor, *J. Phys. Chem. C*. 115 (2011) 282–287. doi:10.1021/jp107812w.
- [34] S. Bai, W. Wu, Y. Qin, N. Cui, D.J. Bayerl, X. Wang, High-Performance Integrated ZnO Nanowire UV Sensors on Rigid and Flexible Substrates, *Adv. Funct. Mater.* 21 (2011) 4464–4469. doi:10.1002/adfm.201101319.
- [35] T.H. Gfroerer, Photoluminescence in Analysis of Surfaces and Interfaces, in: *Encycl. Anal. Chem.*, John Wiley & Sons, Ltd, 2006. doi:10.1002/9780470027318.a2510.
- [36] M.H. Habibi and B. Karimi, Synthesis and Reactivity in Inorganic, Metal-Organic, and Nano-Metal Chemistry **44**, 1291 (2014). C. Periasamy, R. Prakash, and P. Chakrabarti, *J Mater Sci: Mater Electron* **21**, 309 (2010).

- [37] G. Bajpai, T. Srivastava, N. Patra, I. Moirangthem, S.N. Jha, D. Bhattacharyya, S. Riyajuddin, K. Ghosh, D.R. Basaula, M. Khan, S.-W. Liu, S. Biring, and S. Sen, *RSC Adv.* **8**, 24355 (2018).
- [38] S. C. Dixon, D. O. Scanlon, C. J. Carmalt, and I. P. Parkin, *J. Mater. Chem. C* **4**, 6946 (2016)
- [39] T. Srivastava, A. Sadanandan, G. Bajpai, S. Tiwari, R. Amin, M. Nasir, S. Kumar, P.M. Shirage, S. Biring, and S. Sen, *Ceramics International* **43**, 5668 (2017).
- [40] S. Tiwari, G. Bajpai, T. Srivastava, S. Viswakarma, P. Shirage, S. Sen, and S. Biring, *Scripta Materialia* **129**, 84 (2017).
- [41] R. Kirste, Y. Aksu, M.R. Wagner, S. Khachadorian, S. Jana, M. Driess, C. Thomsen, and A. Hoffmann, *Chemphyschem* **12**, 1189 (2011).
- [42] V.I. Korepanov, S.-Y. Chan, H.-C. Hsu, and H. Hamaguchi, *Heliyon* **5**, e01222 (2019).
- [43] J.W. Tringe, H.W. Levie, S.K. McCall, N.E. Teslich, M.A. Wall, C.A. Orme, and M.J. Matthews, *Appl. Phys. A* **109**, 15 (2012).
- [44] S. Tiwari, G. Bajpai, T. Srivastava, S. Viswakarma, P. Shirage, S. Sen, and S. Biring, *Scripta Materialia* **129**, 84 (2017).
- [45] R. Kirste, Y. Aksu, M.R. Wagner, S. Khachadorian, S. Jana, M. Driess, C. Thomsen, and A. Hoffmann, *Chemphyschem* **12**, 1189 (2011).

- [46] V.I. Korepanov, S.-Y. Chan, H.-C. Hsu, and H. Hamaguchi, *Heliyon* **5**, e01222 (2019). J.W. Tringe, H.W. Levie, S.K. McCall, N.E. Teslich, M.A. Wall, C.A. Orme, and M.J. Matthews, *Appl. Phys. A* **109**, 15 (2012).
- [47] C.F. Windisch, G.J. Exarhos, C. Yao, and L.-Q. Wang, *Journal of Applied Physics* **101**, 123711 (2007).
- [48] S. Ayaz, P. Mishra, and S. Sen, *Journal of Applied Physics* **126**, 024302 (2019).
- [49] P.K. Mishra, S. Ayaz, T. Srivastava, S. Tiwari, R. Meena, B. Kissinquincker, S. Biring, and S. Sen, *J Mater Sci: Mater Electron* **30**, 18686 (2019).
- [50] R. Yogamalar, P.S. Venkateswaran, M.R. Benzigar, K. Ariga, A. Vinu, and A.C. Bose, *J. Nanosci. Nanotech.* **12**, 75 (2012).
- [51] E. Monroy, F.O. s, and F. Calle, *Semicond. Sci. Technol.* **18**, R33 (2003).
- [52] M.N.H. Mia, M.F. Pervez, M.K. Hossain, M. Reefaz Rahman, M.J. Uddin, M.A. Al Mashud, H.K. Ghosh, and M. Hoq, *Results in Physics* **7**, 2683 (2017).
- [53] T. Srivastava, S. Kumar, P. Shirage, and S. Sen, *Scripta Materialia* **124**, 11 (2016).
- [54] T.L. Tan, C.W. Lai, and S.B. Abd Hamid, *Journal of Nanomaterials* **2014**, 1 (2014).
- [55] M.-C. Huang, J.-C. Lin, S.-H. Cheng, and W.-H. Weng, *Surf. Interface Anal.* **49**, 434 (2017).

- [56] T. Srivastava, G. Bajpai, N. Tiwari, D. Bhattacharya, S.N. Jha, S. Kumar, S. Biring, and S. Sen, *Journal of Applied Physics* **122**, 025106 (2017).
- [57] I. Sorar, D. Saygin-Hinczewski, M. Hinczewski, and F.Z. Tepehan, *Applied Surface Science* **257**, 7343 (2011).
- [58] O. Belahssen, H. Ben Temam, S. Lakel, B. Benhaoua, S. Benramache, and S. Gareh, *Optik* **126**, 1487 (2015).
- [59] R.C. Rai, *Journal of Applied Physics* **113**, 153508 (2013).
- [60] D. Dimova-Malinovska, H. Nichev, and O. Angelov, *Physica Status Solidi c* **5**, 3353 (2008).
- [61] H. Chen, J. Ding, W. Guo, G. Chen, and S. Ma, *RSC Adv.* **3**, 12327 (2013).
- [62] E. Musavi, M. Khanlary, and Z. Khakpour, *Journal of Luminescence* **216**, 116696 (2019).
- [63] R. Khokhra, B. Bharti, H.-N. Lee, and R. Kumar, *Sci Rep* **7**, (2017).
- [64] S. Lee, Y. Lee, and G.N. Panin, *ACS Appl. Mater. Interfaces* **9**, 20630 (2017).
- [65] E.G. Barbagiovanni, V. Strano, G. Franzò, I. Crupi, and S. Mirabella, *Appl. Phys. Lett.* **106**, 093108 (2015).
- [66] A.B. Djurišić, Y.H. Leung, K.H. Tam, L. Ding, W.K. Ge, H.Y. Chen, and S. Gwo, *Appl. Phys. Lett.* **88**, 103107 (2006).

- [67] A.F. Kohan, G. Ceder, D. Morgan, and C.G. Van de Walle, *Phys. Rev. B* **61**, 15019 (2000).
- [68] F. Oba, S.R. Nishitani, S. Isotani, H. Adachi, and I. Tanaka, *Journal of Applied Physics* **90**, 824 (2001).
- [69] S.B. Zhang, S.-H. Wei, and A. Zunger, *Phys. Rev. B* **63**, 075205 (2001).
- [70] K.E. Knutsen, A. Galeckas, A. Zubiaga, F. Tuomisto, G.C. Farlow, B.G. Svensson, and A. Kuznetsov, *Physical Review B. Condensed Matter and Materials Physics* **86**, (2012).
- [71] T. Wu, A. Wang, L. Zheng, G. Wang, Q. Tu, B. Lv, Z. Liu, Z. Wu, and Y. Wang, *Sci Rep* **9**, 17393 (2019).
- [72] F. Hai-Bo, Y. Shao-Yan, Z. Pan-Feng, W. Hong-Yuan, L. Xiang-Lin, J. Chun-Mei, Z. Qin-Sheng, C. Yong-Hai, and W. Zhan-Guo, *Chinese Phys. Lett.* **24**, 2108 (2007).
- [73] S.A. Ansari, M.M. Khan, S. Kalathil, A. Nisar, J. Lee, and M.H. Cho, *Nanoscale* **5**, 9238 (2013).
- [74] Y. Darma, T. Seng Herng, R. Marlina, R. Fauziah, J. Ding, and A. Rusydi, *Appl. Phys. Lett.* **104**, 081922 (2014).
- [75] J.G. Reynolds and C.L. Reynolds, *Advances in Condensed Matter Physics* **2014**, 1 (2014).
- [76] S. Khachadorian, R. Gillen, S. Choi, C. Ton-That, A. Kliem, J. Maultzsch, M.R. Phillips, and A. Hoffmann, *Physica Status Solidi (b)* **252**, 2620 (2015).
- [77] A. Travlos, N. Boukos, C. Chandrinou, H.-S. Kwack, and L.S. Dang, *Journal of Applied Physics* **106**, 104307 (2009).

- [78] D.M. Hofmann, D. Pfisterer, J. Sann, B.K. Meyer, R. Tena-Zaera, V. Munoz-Sanjose, T. Frank, and G. Pensl, *Appl. Phys. A* **88**, 147 (2007).
- [79] L.E. Halliburton, N.C. Giles, N.Y. Garces, M. Luo, C. Xu, L. Bai, and L.A. Boatner, *Appl. Phys. Lett.* **87**, 172108 (2005).
- [80] G. Juárez-Díaz, J. Martínez, M.L. García-Cruz, R. Peña-Sierra, J.A. García, and M. Pacio, *physica status solidi c* **7**, 957 (2010).
- [81] H. Fukushima, H. Uchida, H. Funakubo, T. Katoda, and K. Nishida, *Journal of the Ceramic Society of Japan* **125**, 445 (2017).
- [82] S.P. Ghosh, K.C. Das, N. Tripathy, G. Bose, D.H. Kim, T.I. Lee, J.M. Myoung, and J.P. Kar, *IOP Conf. Ser.: Mater. Sci. Eng.* **115**, 012035 (2016).
- [83] J. Huang, Y. Du, Q. Wang, H. Zhang, Y. Geng, X. Li, and X. Tian, *Sensors (Basel)* **18**, (2017)
- [84] V. Vaithianathan, B.-T. Lee, and S. S. Kim, *Appl. Phys. Lett.* **86**, 062101 (2005).
- [85] M. Joseph, H. Tabata, and T. Kawai, *Jpn. J. Appl. Phys.* **38**, L1205 (1999).
- [86] C.-Y. Tsay and S.-C. Liang, *J. Alloys Compd.* **622**, 644 (2015).
- [87] F. E. Ghodsi and J. Mazloom, *Appl. Phys. Mater. Sci. Process.* **108**, 693 (2012).
- [88] M.-C. Jun, S.-U. Park, and J.-H. Koh, *Nanoscale Res. Lett.* **7**, 639 (2012).